Title
On the provenance of GEMS, a quarter century post discovery

Authors
Bradley, John P
Ishii, Hope A
Bustillo, Karen
et al.

Publication Date
2022-10-01

DOI
10.1016/j.gca.2022.06.036

Peer reviewed

Geochimica et Cosmochimica Acta 335 (2022) 323–338

Contents lists available at ScienceDirect

Geochimica et Cosmochimica Acta

journal homepage: www.elsevier.com/locate/gca

On the provenance of GEMS, a quarter century post discovery

John P. Bradley [a,*], Hope A. Ishii [a], Karen Bustillo [b], James Ciston [b], Ryan Ogliore [c], Thomas Stephan [d,e], Donald E. Brownlee [f], David J. Joswiak [f]

[a] Hawai'i Institute of Geophysics and Planetology, University of Hawai 'i at Mānoa, 1680 East-West Road, Honolulu, HI 96822, USA
[b] National Center for Electron Microscopy, Molecular Foundry, Lawrence Berkeley National Laboratory, Berkeley, CA 94720, USA
[c] Laboratory for Space Sciences, Washington University, St. Louis, MO 63130, USA
[d] Department of Geophysical Sciences, The University of Chicago, Chicago, IL 60637, USA
[e] Chicago Center for Cosmochemistry, Chicago, IL, USA
[f] Department of Astronomy, University of Washington, Seattle WA 98195, USA

ARTICLE INFO

Article history:
Received 27 January 2022
Accepted 26 June 2022
Available online 5 July 2022
Associate editor: Martin Robert Lee

Keywords:
Interplanetary dust
GEMS
Provenance
Secondary alteration
Presolar
Interstellar
Medium

ABSTRACT

The provenance of GEMS (glass with embedded metal and sulfides) in cometary type interplanetary dust particles is investigated using analytical scanning transmission electron microscopy and secondary ion mass spectrometry. We review the current state of knowledge and closely examine the densities, elemental compositions and distributions, iron oxidation states, and isotopic compositions of a subset of GEMS in chondritic porous interplanetary dust. We find that GEMS are underdense with estimated densities that are 35–65% of compositionally equivalent crystalline aggregates. GEMS low densities result in a lower contribution to the bulk compositions of IDPs than has been assumed based on their volume fraction. We also find that element/Si ratios, assumed to be primary (indigenous), are instead perturbed by contamination and secondary alteration, including pulse heating during atmospheric entry. Fe in pyrrhotite inclusions was oxidized and Mg, S, Ca, and Fe were depleted relative to lithophile Al and Si, resulting in reduction in element/Si ratios. Because they trap outgassing elements, Fe-rich oxide rims that formed on the surface of GEMS are serendipitous "witness plates" to the changes in composition that accompany atmospheric entry. As a result of alteration, GEMS elemental compositions cannot reliably inform about their provenance. Except for highly anomalous oxygen isotope ratios measured in some large GEMS grains that indicate a contribution from circumstellar dust, oxygen isotope compositions are generally poor indicators of provenance. Prior work indicates that most GEMS fall close to the terrestrial oxygen isotope composition, which, however, does not exclude a presolar interstellar origin. Nitrogen isotopic compositions are more diagnostic. Elevated $^{15}N/^{14}N$ ratios indicate that GEMS accreted in conjunction with formation of organic matter by ion–molecule reactions in a cold (<50 K) presolar environment like the extreme outer nebula or interstellar medium. Considering all observations, we conclude that GEMS are most likely processed interstellar silicates.

1. Introduction

The Solar System formed from interstellar gas and dust, most of the solids originally "stardust" generated from the outflows of, e.g., asymptotic giant branch (AGB) stars or supernovae. During its lifetime in the interstellar medium (ISM), stardust is heavily processed by supernovae shocks, collisions, implantation and sputtering by stellar winds, which leads to amorphization, dilution and loss of isotopic memory of parent stars (Zhukovska et al., 2008; Matsura et al., 2011; Altwegg, 2022). When dust cycles into colder, dense ISM regions like molecular clouds, it undergoes additional growth via UV photolysis, condensation of volatile elements, and development of icy organic-bearing mantles on grain surfaces that may participate in sticking and aggregation (Jones, 2016; Jäger et al., 2016; Altobelli et al., 2016; Ishii et al., 2018). The interstellar dust population has an average elemental composition for condensable elements near solar composition (e.g., Ueda et al., 2005; Wiedenbeck, 2013) and is thought to be dominated by dust processed in outflows from AGB stars and supernovae, in the diffuse ISM, and in molecular clouds (Zhukovska et al., 2008, 2018; Jenkins, 2009; Draine, 2009, 2011). Theory (modeling) and observation implicate two principal interstellar dust components, (1) amorphous silicates, based on the shape of the astronomical

* Corresponding author.
E-mail address: jbradley@higp.hawaii.edu (J.P. Bradley).

https://doi.org/10.1016/j.gca.2022.06.036
0016-7037/

~10 μm silicate feature (e.g., Hanner et al., 1998), and (2) some form of carbon, possibly in mantled and composite grains (Dartois and Muñoz-Caro, 2007; Draine, 2011; Jones, 2016; Ysard et al., 2016).

An outstanding question in cosmochemistry and planetary science is whether any of these "Rosetta stones" of the Solar System, that is original unprocessed, amorphous interstellar dust, survive in recognizable form. Circumstellar silicate grains with isotope anomalies genetically linking them to their parent stars are found in primitive (minimally altered) meteorites. Although these grains establish that at least some grains from the ISM survive, they are very rare in meteorites. It is generally assumed that amorphous silicate ISM dust may have survived in cold regions but was mostly destroyed in hot regions in the solar nebula, either during initial accretion into the protosolar/protoplanetary disk or during high-temperature processes such as those that formed chondrules and calcium–aluminum-rich inclusions (CAIs). To date, no isotopically anomalous circumstellar silicate grain in any meteorite has been rigorously identified as amorphous, due in part to insufficient characterization. Although several authors have claimed to identify amorphous presolar silicates in primitive meteorites, many of those observations are based on non-stoichiometric elemental chemistry, and when transmission electron microscopy (TEM) has been performed, it nearly always followed nanoscale secondary ion mass spectrometry (NanoSIMS) analysis that amorphizes the top ~10–30 nm of the grain of interest and often followed focused ion beam isolation of the grains, which also amorphizes silicates (Nguyen et al., 2016; Floss and Haenecour, 2016). (For a more thorough discussion about identification of circumstellar amorphous silicates in meteorites, see Ohtaki et al., 2021.) It is possible that amorphous presolar silicates are present in meteorites but need to be more rigorously characterized. Alternatively, amorphous silicate ISM dust may have been altered beyond recognition by thermal metamorphism and aqueous alteration, accompanied by perturbation of isotope ratios, and leading to the formation of layer silicates in meteorite parent bodies. Amorphous silicates may be expected to better survive in frozen comet parent bodies that accreted in the outer regions of the protoplanetary disk where heating effects were lower. Amorphous silicates were identified in returned samples from the only comet sample return mission to date NASA's Stardust mission to comet 81P/Wild 2; however, the silica aerogel capture medium prevented unambiguous distinction between the products of hypervelocity capture and indigenous amorphous silicates (Ishii et al., 2008; Ishii, 2019). Abundant amorphous silicates, some with measurable isotope anomalies, are found in anhydrous interplanetary dust particles (IDPs) and some micrometeorites (MMs) that are collected in the stratosphere and in Antarctic snow and ice.

In this paper, we synthesize new and existing data to assess amorphous silicate grains in IDPs and MMs. The exotic properties of these grains match known and inferred properties of interstellar silicate dust (Goodman and Whittet, 1995; Martin, 1995; Kimura, 2017; Hensley and Draine, 2021). The grains, known as GEMS (glass with embedded metal and sulphides[1]) are found in IDPs and MMs classified as "chondritic porous" (CP) because they have chondritic (solar) bulk compositions within a factor of ~2. CP IDPs are extremely fragile, sometimes porous, aggregates of GEMS, crystalline minerals, and organic carbon (Fig. 1, see Supplementary Material, Fig. S2) (Bradley, 2014; Dobrică et al., 2012; Noguchi et al., 2017). GEMS are exotic and unique among known meteoritic materials; most are nanoporous and rounded, with a well-defined size range (typically 0.1–0.5 μm). They are comprised of a simple three-component assemblage of nanometer-sized metal and sulfide inclusions in amorphous silicate matrix, and they are the only known submicrometer-sized extraterrestrial bodies with nanogram-to-femtogram masses and approximately solar compositions for the rock-forming elements. The earliest observations of GEMS were made with instrumentation incapable of detecting elements with Z < 11 (Na) and, based on their low contrast and matrix texture in transmission electron micrographs, they were assumed to be carbon-rich "tarballs" (Bradley, 1984). Subsequent acid-dissolution experiments and improvements in analytical capability led to the discovery that GEMS contain both silica-rich and carbon-rich components (Bradley, 1994a; Dai et al., 2002; Ishii et al., 2018). In most CP IDPs, we observe that GEMS account for 20–40% of the volume, although in some IDPs, especially carbon-rich ones, they dominate the volume (e.g., Fig. 1). They are present only in IDPs and MMs that are anhydrous and chondritic, strongly suggesting a relationship to small, frozen parent bodies, like comets and perhaps some asteroids.

The compositions of GEMS are notable; they cluster around chondritic (solar) composition. Average element/Si ratios are systematically weakly depleted, although individual element/Si ratios among GEMS can vary by almost an order of magnitude (Ishii et al., 2008; Dobrică et al., 2012; Keller and Messenger, 2011) (Fig. S1, see Supplementary Material). Electron diffraction identifies the metal inclusions as body-centered cubic kamacite (Fe^0Ni^0) and the sulfides as hexagonal pyrrhotite ($[Fe^{2+}Ni^{2+}]S$) with Ni/Fe ≈ 0.1 (Bradley, 1994b, 2020; Dai and Bradley, 2001).

On the assumption that most GEMS grains are pristine and escaped significant post-accretional alteration, two very different origins have been proposed: (a) formation in a cold (<50 K) ISM or outer solar nebula environment, and (b) condensation from a hot (>1000 K) gas in the solar nebula. The cold origin hypothesis is based on evidence of irradiation exposure and accretion in a low-temperature (<50 K) environment(s) and on the overlap of GEMS' exotic properties, known and inferred, with those of interstellar amorphous silicate grains; for example, both GEMS and interstellar amorphous silicates are rounded with superparamagnetic inclusions. Superparamagnetic metal and pyrrhotite inclusions in GEMS provide an explanation for the observed alignment of interstellar dust (amorphous silicates) in the galactic magnetic field (Goodman and Whittet, 1995; Martin, 1995; Hoang and Lazarian, 2016; Zhukovska et al., 2018). Furthermore, the ~10 μm infrared silicate feature of GEMS matches the position and shape of the ~10 μm silicate feature of interstellar dust as well as amorphous dust in some outer accretion disks (Bradley, 1994a; Bradley et al., 1999; Keller et al., 2000; van Boekel et al., 2004, 2005). Some GEMS are indisputably of interstellar origin: They have anomalous oxygen isotopic compositions (Messenger et al., 2003; Floss et al., 2006). Anomalous GEMS tend to be on the larger end of the GEMS size distribution, suggesting that dilution by surrounding material in spatial resolution-limited isotope imaging may obscure anomalies in smaller GEMS. The rest of the GEMS population is otherwise identical in all other properties to those isotopically anomalous GEMS, so it is logical to consider an interstellar origin for the entire population (Bradley and Ishii, 2008). If presolar in origin, GEMS would be the source of much of the condensed matter from which the Solar System and other planetary systems formed (Bradley, 1994a; Goodman and Whittet, 1995; Martin, 1995). The hot origin hypothesis is based on chemical compositions of GEMS, specifically sub-solar element/Si ratios, that are assumed to be indigenous and complementary to element/Si ratios of crystalline components in CP IDPs; the hypothesis posits, by implication, that both GEMS and crystals formed together in the same (solar nebula) reservoir (Keller and Messenger, 2011). Attempts to synthesize GEMS in the laboratory are inconclusive: Both high-temperature vapor phase and low-temperature irradia-

[1] The term GEMS is used to refer to both singular and plural GEMS grains, depending on context, in this work.

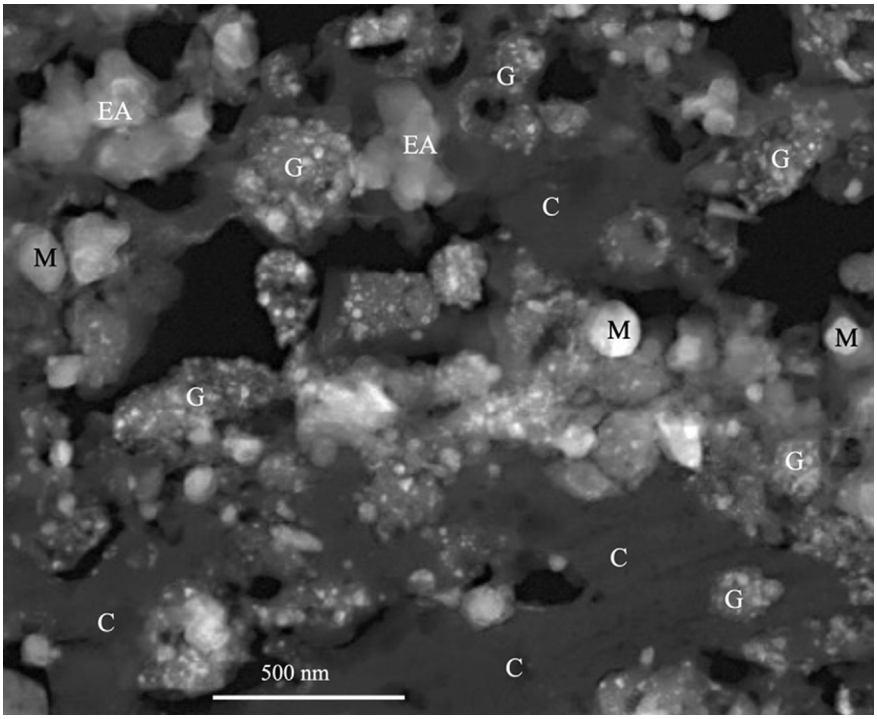

Fig. 1. Darkfield image of GEMS (G), single-mineral crystals (M), and equilibrated aggregates (EAs) embedded in organic carbon matrix (C) from IDP fragment LT29.

tion synthesis experiments have been performed, with neither experimental approach fully reproducing GEMS' properties (e.g., Jäger et al., 2016; Matsuno et al., 2022).

Because GEMS are high surface-area and mostly amorphous nanomaterials, they are inherently predisposed to secondary alteration. As such, exclusive reliance on chemical (elemental) composition to establish GEMS' provenance requires determining whether they have been modified prior to and during ~4.6 Ga residence within cold, often cometary parent bodies, followed by exposure as small particles orbiting the Sun (Bradley et al., 1984), frictional heating when entering the Earth's atmosphere, and exposure to terrestrial contamination. We exploit recent advances in analytical electron microscopy, specifically combined energy-dispersive X-ray spectroscopy and electron energy-loss spectroscopy and spectrum imaging to map, for the first time, both the compositions *and* (Fe) oxidation states in the same GEMS with single-nanometer-scale spatial resolution to examine the sometimes-subtle effects of secondary alteration in individual GEMS. We also estimate the atomic density of GEMS relative to similar composition crystal assemblages. We then evaluate the significance and causes of the sub-solar element/Si ratios reported in the literature and assess the assumption of complementarity between GEMS and single-mineral crystals in IDPs. Finally, we measure the isotopic compositions of organic carbon within and encapsulating GEMS and assess the implications of nitrogen and oxygen isotope compositions for the provenance of GEMS.

2. Experimental methods

Since GEMS are nanomaterials, analytical techniques and instrumentation capable of nanometer spatial resolution are required to determine their compositions, structures, and mineralogy. As such, we use TEM and associated spectroscopy methods and NanoSIMS. These methods were applied to IDPs containing GEMS and to (nano)porous and non-porous silica.

2.1. Samples and preparation

For assessment of correlated composition and (Fe) oxidation state, we include GEMS from several (organic-)carbon-rich IDPs (see Supplementary Material Fig. S2). Since organic carbon is susceptible to thermal decomposition and ablative loss during atmospheric entry, providing at least some protection against thermal oxidation, carbon rich IDPs are less likely to have been strongly heated. However, organic carbon also acts as a sponge for terrestrial contaminants like silicone oil, the capture medium on (IDP) collection substrates flown on high-altitude aircraft. The following IDPs were studied: U217B19 is a 6 μm × 9 μm CP IDP. LT29 and LT30, with diameters of ~17 and ~15 μm, respectively, are low-porosity constituents of an IDP, first recognized as organic carbon-rich by characteristic red-brown color in transmitted light (see Supplementary Material Fig. S2). LT29 and LT30 were removed from among fragments of the cluster IDP U220GCA, which is by far the largest IDP collected in the stratosphere to date with an estimated pre-collection size of ~500 μm (Bradley, 2014). Both clasts contain abundant GEMS (e.g., Fig. 1). U219C11 is a typical, less carbon-rich IDP that contains similar volumes of GEMS and crystalline single-mineral grains, and U2011B10 was collected on an (oil-free) polyurethane collector (Messenger et al., 2015). Most samples were embedded in elemental sulfur (S) or epoxy and sectioned using an ultramicrotome equipped with a diamond knife. Fracturing, or "chatter", in ultramicrotomed thin sections is often observed on spatial scales >1 μm in coarse-grained, crystalline specimens, but most IDPs that are dominated by GEMS and organic carbon are relatively soft (non-brittle) and extremely fine-grained so that intact thin sections free of significant chatter and without significant thickness variation can be produced. The sections, 75–100 nm in thickness, were transferred to thin-film carbon substrates on copper and gold mesh TEM support grids. One section of U217B19 was analyzed for isotopic compositions.

For assessment of GEMS' densities, ultramicrotomed sections were analyzed of a carbon-rich fragment of IDP U220GCA, of

U217B19, and of an additional anhydrous IDP, W7027A 8D, with typical carbon content and dimensions of 6 μm × 9 μm. To illustrate the effect of differing density on intensity of X-ray emission, nano-porous silica (SiO_2) aerogel and neighboring non-porous silica generated by melting and quenching of aerogel during impact capture of comet dust (NASA Stardust sample C2115,33,123,0,0) were analyzed.

2.2. Transmission electron microscopy

We acquired high-angle annular dark-field (HAADF) and bright-field images of GEMS at magnifications between 5000× and 50,000× using three 60–300 keV Titan (scanning) transmission electron microscopes. See Supplementary Material for details of microscopes and associated spectrometers. We measured compositions and oxidation states using energy-dispersive X-ray spectroscopy (EDX) and electron energy-loss spectroscopy (EELS), respectively. Combined EDX/EELS spectrum imaging was employed to show the spatial distribution of elements, oxidation states, and chemical bonding at single nanometer spatial scales.

2.2.1. Energy-dispersive X-ray spectroscopy

Spectrum imaging of GEMS was performed using a Titan equipped with four windowless EDX detectors with a total solid angle of 0.7 sr. The spectrum images show the spatial distributions of all displayed elements. They were acquired using Esprit 1.9 software (Bruker Corporation) to iteratively raster a sub-nanometer diameter electron probe with 1.6 or 3.3 nm pixel intervals, resulting in compositional map frames with full X-ray fluorescence spectra accumulated in each pixel. Spectrum images ranging from 500 to 800 pixels on a side and total acquisition times from 30 to 180 min were acquired at 300 kV, 250–1000 pA beam currents, and a dispersion of 10 eV/pixel. Before and after HAADF images as well as back-to-back maps were acquired to rule out significant alteration of the specimens during mapping. The Esprit software presents element distributions in color-coded maps around characteristic K-edge X-ray energies for each element. EDX spectrum images are for visualization of spatial distributions only and are not accurate representations of quantitative composition. Element abundances were quantified from spectra summed over selected regions and normalized to 100 at.%. Background removal, fitting and standardless quantification were performed using the Esprit 1.9 software with factory-calibrated k-factors. On mineral standards of olivine, pyroxene, kamacite, and pyrrhotite, it provides major element compositions with 1–2% relative uncertainty and minor element compositions with 3–7% relative uncertainty, depending on relative abundances.

2.2.2. GEMS densities

The densities of nanoporous silica (SiO_2) aerogel relative to non-porous melt-quenched silica, and of GEMS relative to equilibrated aggregates (EAs), were estimated using X-ray emission counts from EDX spectra of ultramicrotomed thin sections. EAs that are found in CP IDPs are non-porous, polycrystalline grains with stoichiometric mineral compositions, and well-defined grained boundaries, some with triple points consistent with crystallization from a melt (Bradley, 1994b). EDX spectra for density estimates were collected at 200 kV with beam currents between 200 and 700 pA and 10 eV/pixel dispersion on two Titan microscopes, one with a single thin-window EDX detector and one with four windowless EDX detectors (see Supplementary Material). To illustrate the methodology, regions of equal area of silica aerogel and neighboring melt-quenched silica were mapped sequentially with equal total dwell time per pixel and electron beam current variation of <2%. Immediately adjacent components in the same ultramicrotomed section have approximately equal thickness, and we conservatively estimate that thickness could differ by <10%. Since equal areas are mapped in each component (silica aerogel and melt-quenched silica), the regions also have the same volume to within <10%. Silica aerogel and melt-quenched silica have identical composition, so differences in total X-ray counts can be attributed to density differences with conservatively estimated uncertainties of ±5% for density ratios. IDPs were similarly mapped by EDX, and regions in individual GEMS grains and in neighboring crystalline EAs of similar composition were analyzed. GEMS grains that show no evidence of atmospheric entry heating (vesiculated carbon, magnetite, partial sintering, sulfide beads on the surface) were targeted, although one grain showing rounding of constituents and volatile loss was included. EAs are small, show no evidence of microtome chatter, and are in close proximity to the GEMS to which they are compared. In some cases, mapping of a larger EA area than GEMS area was necessary to best match the composition of the neighboring GEMS grains, and in such cases, total X-ray counts from each GEMS region were scaled by the ratio of the pixels in that GEMS region to the pixels in the accompanying EA region in order to allow comparison of total X-ray signal from equivalent volumes and analysis times of GEMS and EAs with similar composition. To address the compositional differences between GEMS and neighboring EAs, we compared the difference in the total counts in spectra of the GEMS compared to those in the spectra of their neighboring EA after scaling to equal Si peak height. Based on that difference, we estimate that uncertainty in the ratios of total X-ray counts due to compositional differences is <±10%. This uncertainty combines in quadrature with the (independent) uncertainty associated with thickness to produce ±11% uncertainty in a single GEMS to EA density ratio.

2.2.3. Electron energy-loss spectroscopy

Oxidation state measurements and spectrum imaging were performed at 300 kV using a Titan microscope equipped with a monochromator, chromatic and spherical aberration correctors, and a GIF Continuum energy filter (Gatan Inc) with a K3 direct (electron) detection CMOS camera operating in counting mode enabling highest signal-to-noise, counting statistics critical, and highest signal-to-noise EELS imaging and spectroscopy at low electron dose. Spectrum images were collected with a 17 mrad convergence semiangle and 54 mrad collection semiangle into the spectrometer. Probe currents of 100–150 pA were used for these measurements with probe sampling at 1 and 2 nm with dwell times of 50 ms per probe position. Sequential spectrum images confirmed no oxidation of the sample during analysis. Because the focused probe (0.1 nm) was smaller than the pixel sampling interval (1–2 nm) for the EELS spectrum images, the electron probe was rastered on a 16 × 16 grid during the 50 ms EELS acquisition at each spectrum image pixel to spread the electron dose over a larger sample area and to integrate the full volume of each 1 or 2 nm region. Spectrum images were compensated for any energy shifts in the position of the zero (energy) loss peak (ZLP) during the scan using DualEELS, which acquires simultaneous spectra over the ZLP and selected higher energy loss regions (Tencé et al., 2006; Scott et al., 2008). The core loss spectrum images were also deconvoluted pixelwise using the simultaneously acquired ZLP at every probe location. The (EELS) spectrum images of Fe oxidation state distributions were generated from Fe-$L_{2,3}$ core scattering edges following Multiple Linear Least Squares (MLLS) fitting of the individual spectra using metal (kamacite) and sulfide (pyrrhotite) as internal standards for Fe^0, Fe^{2+}, as well as external metal (Fe^0), Fe^{2+}, and Fe^{3+} oxide standards (Leapman and Swyt, 1988; see Fig. S3 in Supplementary Material).

2.3. Secondary ion mass spectrometry

A Cameca NanoSIMS 50 was used to analyze hydrogen, carbon, nitrogen, and oxygen isotopes in a Pt-supported, ~75 nm thick,

ultramicrotomed section of IDP U217B19 that is composed mostly of organic carbon and GEMS with minimal crystalline components (details in Ishii et al., 2018). A primary beam of Cs^+ ions (~1 pA beam current, 16 keV total impact energy), focused to ~75 nm and rastered over 10 × 10 μm^2, was used for all measurements. First, carbon and nitrogen isotopes were measured simultaneously. Five electron multipliers measured $^{12}C^-$, $^{13}C^-$, $^{12}C^{14}N^-$, $^{12}C^{15}N^-$, and $^{28}Si^-$. Data was recorded as scanning ion images of 256 × 256 pixels. Next, carbon and oxygen isotopes were measured as $^{12}C^-$, $^{13}C^-$, $^{16}O^-$, $^{17}O^-$, $^{18}O^-$. Finally, hydrogen isotopes were measured as H^-, D^-. Secondary electron images were recorded simultaneously for all measurements. Scanning ion images were analyzed with Matlab code, which is included in Research Data. Isotope ratios are normalized to the whole particle composition, which is assumed to be "normal" (i.e., terrestrial).

3. Results

We assessed the density of GEMS using the total X-ray counts obtained by EDX (Fig. 2 and Table 1). For analyses of samples with identical compositions over equal sample volume (thickness times surface area) and measurement duration, a difference in total X-ray counts is attributable to a difference in atomic density, as demonstrated by the spectra in Fig. 2b from silica aerogel and silica glass. Table 1 shows the ratio of total X-ray counts from silica aerogel to silica glass is 0.34–0.37, so density of the aerogel is ~34–37% of that of the silica glass. (This nanoporous Stardust aerogel was compressed to concentrate comet-dust-rich regions of the track. A ratio of ~0.01–0.02 would be expected from uncompressed aerogel.) Table 1 also shows the ratio of total counts from 20 GEMS relative to EAs from three anhydrous IDPs, collected over equivalent volumes and analysis times. EAs are polycrystalline and thus expected to be fully dense. Each pair of regions in GEMS and EA have very similar, albeit not identical, compositions so that the ratio of total X-ray counts between them provides a reasonable estimate of the ratio of their atomic densities. Fig. 2d compares (equal volume, equal time) EDX spectra of an EA and a GEMS grain in IDP W7207A 8D. The GEMS grain in Fig. 2d is, for example, more Fe- and C-rich than the EA; however, the samples are ultramicrotomed thin sections for which differential absorption is not very significant and the Cliff-Lorimer thin film approximation holds well. (It should be noted that higher Fe content contributes to greater total X-ray counts, but any resultant differential absorption of C and O X-rays would counteract that effect by reducing C and O contribution to the total X-ray counts.) As described in Section 2.2.2, we estimate a ±11% uncertainty for each GEMS to EA ratio. The ratio of total counts from GEMS to EA in this example is 0.54, so this GEMS grain has an atomic density on the order of 54 ± 11%. of its neighboring EA. The average ratio of total X-ray counts of GEMS to EA from all GEMs and EA pair analyzed in Table 1 is 0.52 ± 0.16 (where the uncertainty is given as the standard deviation, which is larger than the standard error of the mean). One GEMS grain marked by an asterisk in Table 1 showed evidence of heating: rounding of constituents and volatile loss. Omitting that GEMS grain, the average ratio is 0.50 ± 0.15. Estimated GEMS densities of ~35–65% of corresponding silicate crystals are consistent with differences observed in HAADF contrast.

Bright-field, dark-field, and EDX spectrum images reveal the mineralogy, petrography and elemental compositions of individual GEMS (Figs. 3–7). In Figs. 3a and 4a, the inclusions are bright in the atomic number (Z)-contrast dark-field images, because they contain higher average atomic-number elements Fe and Ni in metal and sulfide inclusions. Lower atomic number elements O, Mg, Al, Ca, and Si are localized in the amorphous silicate matrix, and no obvious alteration of the matrix is observed. Although S, Fe, and

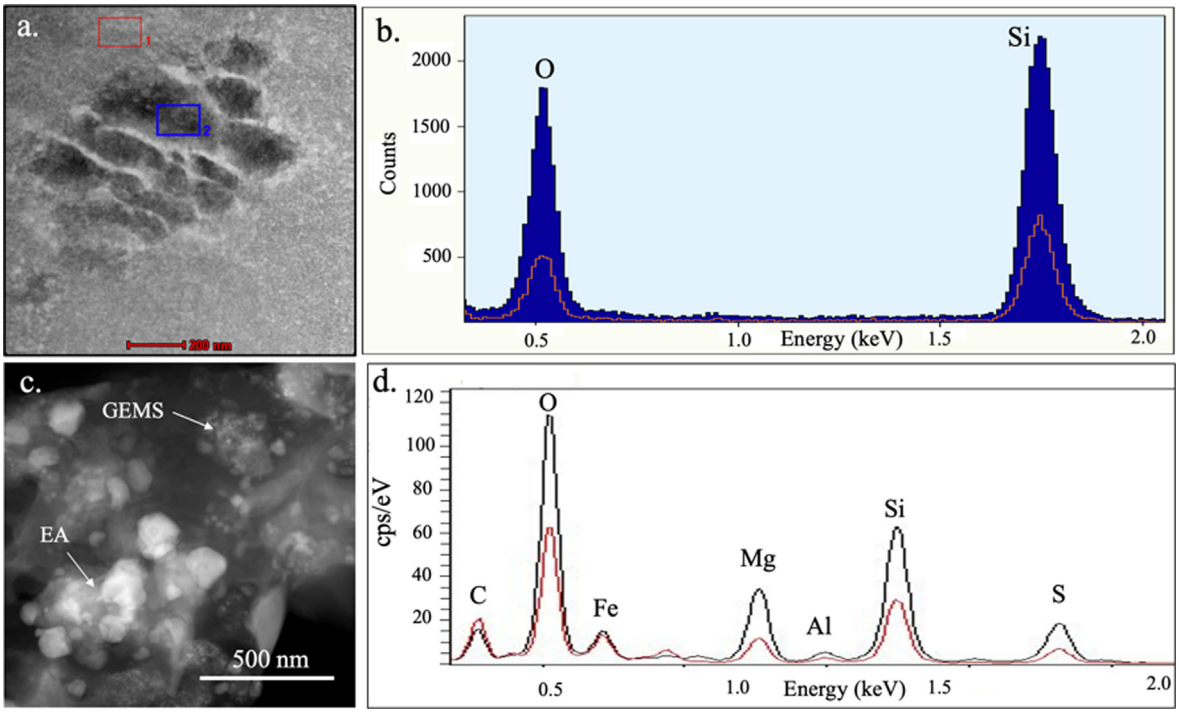

Fig. 2. X-ray intensity from less and more dense regions. (a) Brightfield image of a region of Stardust impact track C2115,33,123,0,0 containing nanoporous silica (SiO_2) aerogel and nonporous melt-quenched silica glass. Scale bar is 200 nm. (b) Spectra from equal volumes of aerogel and glass. The red line spectrum corresponds to aerogel in region 1, and the blue solid spectrum, to glass in region 2 (rectangles in (a)). Differences in X-ray fluorescent intensity are due to density. (c) Darkfield image of GEMS and a neighboring equilibrated aggregate in IDP W7207A 8D. (d) EDX spectra from equal volumes of a crystalline equilibrated aggregate (EA) (black) and the neighboring GEMS grain (red). Despite nearly identical compositions (element/Si ratios), total of X-ray counts from the GEMS is 0.54 ± 0.11× that from the EA. Elemental compositions obtained from the spectra in (d) are given in Table 2.

Table 1
Ratio of total X-ray counts from compressed aerogel and from neighboring melt-quenched silica, and ratio of total X-ray counts from 20 GEMS and from neighboring EAs in three IDPs. The GEMS whose ratio is marked by a * showed evidence of heating in rounding of constituents and volatile loss.

	Region 1	Region 2						
silica aerogel	0.37	0.34						
	GEMS 1	GEMS 2	GEMS 3	GEMS 4	GEMS 5	GEMS 6	GEMS 7	GEMS 8
W7207A 8D	0.54	0.57	0.49	0.48				
U217B19	0.85*	0.63	0.47	0.66	0.39	0.54	0.44	0.45
U220GCA	0.48	0.92	0.33	0.31	0.56	0.24	0.52	0.52

Average ratio of total X-ray counts (GEMS / EA) for all GEMS: 0.52 ± 0.16.
Average ratio of total X-ray counts (GEMS / EA) excluding U217B19 GEMS 1: 0.50 ± 0.15.

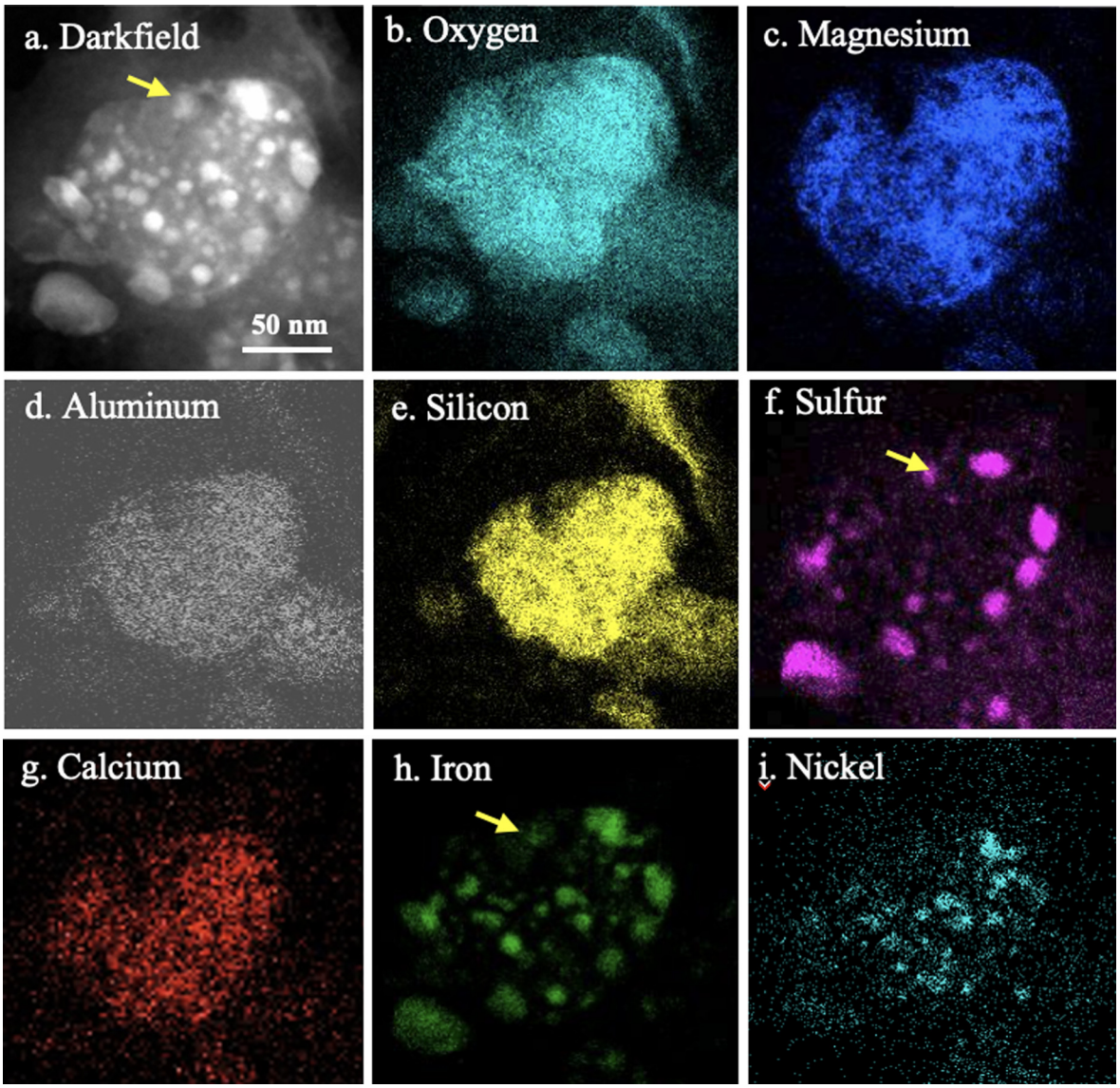

Fig. 3. A GEMS grain in LT29 showing alteration of inclusions. (a) Darkfield image and (b–i) corresponding EDX spectrum images showing the spatial distributions of O, Mg, Al, Si, S, Ca, Fe, and Ni. See text for discussion of arrowed sulfide. Decoupling of Ni from Fe and S in sulfides and surface ripening and decoration of (Ni-depleted) sulfides (see f, h, i,) likely occur during atmospheric entry heating. See also Fig. 4.

Ni are highly concentrated within the inclusions, there is evidence of significant alteration of inclusions. One of the sulfide inclusions (arrowed in Fig. 3a, f & h) that preferentially decorate the grain surface is almost completely eroded away with loss of S and Fe. Iron in the metal and sulfide inclusions is nominally in the 0 and +2 oxidation states, respectively, but the EELS Fe-$L_{2,3}$ core scattering edge and spectrum imaging indicate that the sulfides are oxidized, as are the surfaces of metal inclusions (Fig. 4). The bulk elemental composition of the grain is given in Table 2.

More advanced alteration is evident in other GEMS. In Fig. 5, the spatial distributions of Al and Si are similar (Fig. 5d & e), but Mg and Ca are decoupled from Al and Si and distributed towards the

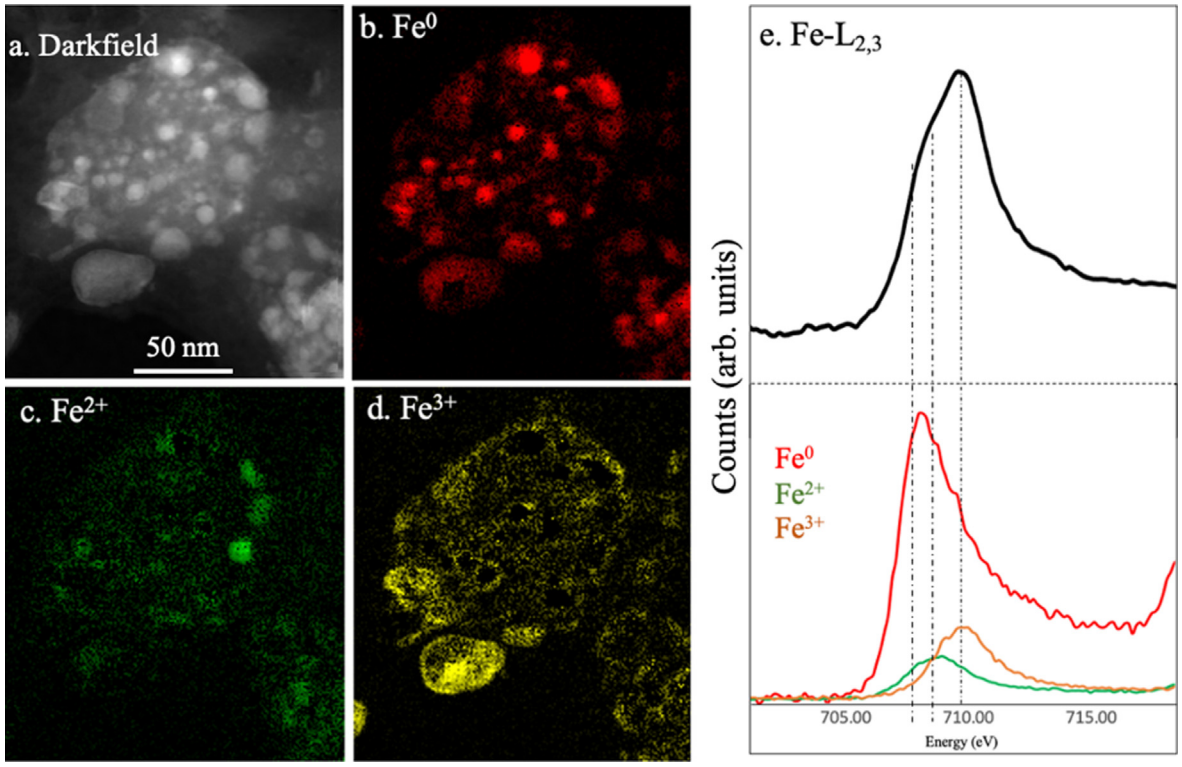

Fig. 4. A GEMS grain in LT29 showing oxidation of inclusions. (a). Darkfield image (also shown in Fig. 3a) and (b–d) corresponding EELS spectrum images showing the spatial distributions of Fe^0, Fe^{2+}, and Fe^{3+}. (e) Fe-$L_{2,3}$ core scattering edge (top) and (Fe^0, Fe^{2+}, Fe^{3+}) edges extracted by MLLS fitting and integrated over the total scan area (bottom).

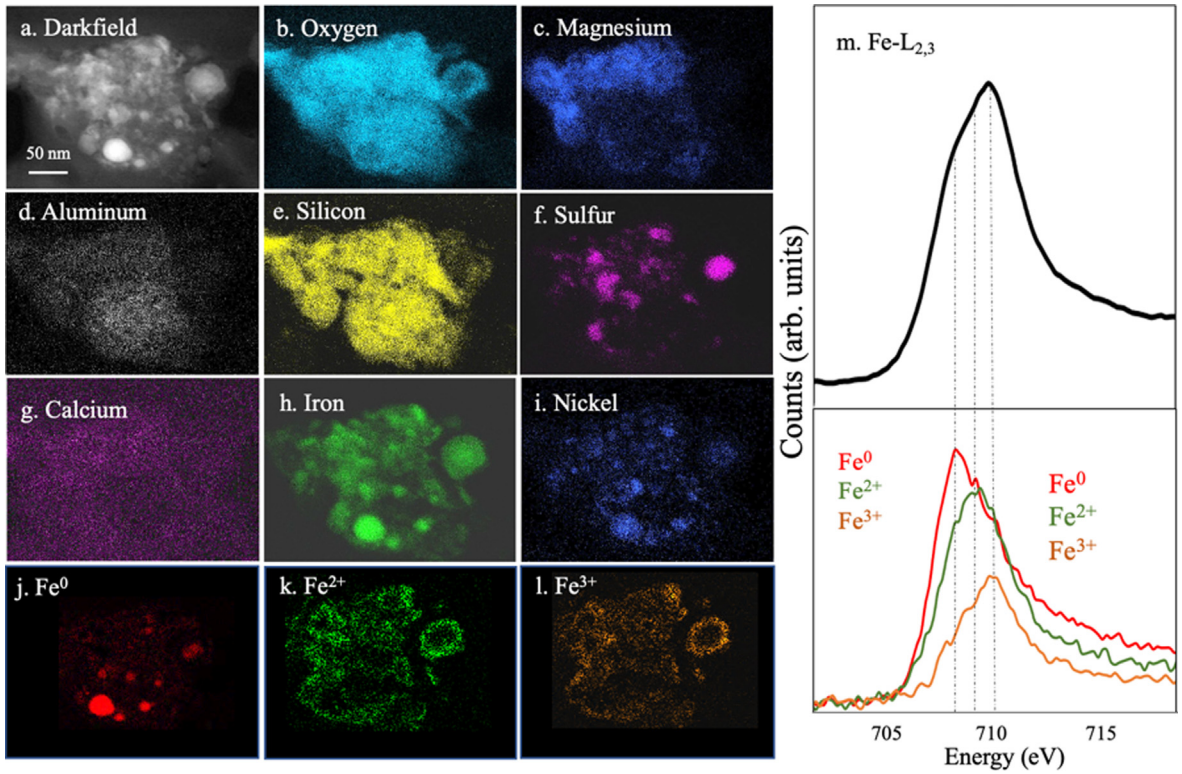

Fig. 5. A GEMS grain in U2011B10 showing oxidation and chemical alteration. (a) Darkfield image and (b–i) corresponding EDX spectrum images showing the spatial distributions of O, Mg, Al, Si, S, Ca, Fe, and Ni. Scale bar is 50 nm and applies to all element distributions. (j–l) EELS spectrum images showing the spatial distributions of Fe^0, Fe^{2+}, and Fe^{3+}. (m) Fe-$L_{2,3}$ core scattering edge (top) and MLLS-fitted (Fe^0, Fe^{2+}, Fe^{3+}) edges (lower right).

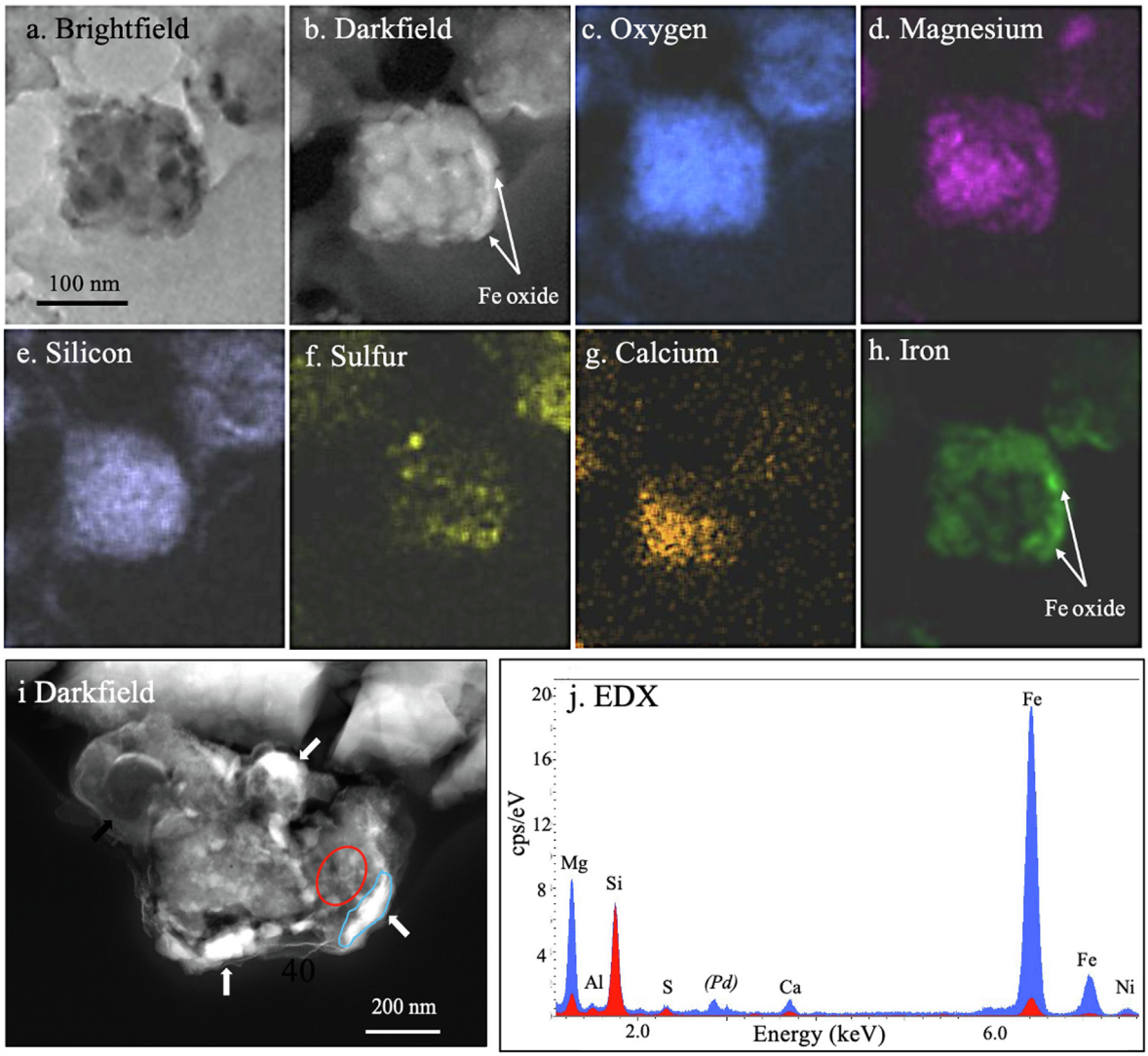

Fig. 6. GEMS grains showing oxidation rims. (a–h) Brightfield, darkfield (HAADF) and EDX spectrum images showing the distribution of O, Mg, Si, S, Ca, and Fe in a GEMS grain in LT29 with rim on a leading surface formed by pulse heating during atmospheric entry. Scale bar in (a) applies to all element distributions. (i & j) Darkfield image of another GEMS grain in LT30 with prominent rim (arrowed), and EDX spectra (scaled to equal Si peak heights) comparing the rim (blue) and GEMS' interior (red) compositions of areas marked in the darkfield image. (Palladium (Pd) is a conductive coating applied prior to thin-sectioning of this IDP).

surface of the grain (Fig. 5c & g). S, Fe, and Ni remain spatially correlated, although there is significant diffusion of Fe into the silicate matrix (Fig. 5f, h &j). EELS Fe $L_{2,3}$ edge spectrum images were derived from deconvolved spectra (e.g., Fig. 5m). They indicate that mixed Fe^{2+} and Fe^{3+} oxidation states are present in the matrix and on the surfaces of metal and sulfides inclusions (Fig. 5k–l) and Fe^{0} is present in the metal inclusions (Fig. 5j). The bulk elemental composition of the grain is given in Table 2.

GEMS on the surfaces of IDPs often have partial Fe-rich oxide rims on their surfaces that developed during atmospheric entry. The bright-field and dark-field images in Fig. 6 show that, compared to those in Figs. 3–5, the inclusions in this rimmed GEMS grain appear more diffuse (Fig. 6a–h). EDX spectrum images in Fig. 6 (a–h) show that while O, Si, and Al remain spatially correlated, Fe and Mg are depleted immediately behind the Mg- and Fe-enriched rim at the surface. In other GEMS, the rims are more extensive, element/Si depletions are larger, and the most internally depleted elements (e.g., Mg, Ca, and Fe) are the most enriched in the rim (Fig. 6i & j). We observe that internal depletions and rim enrichments are not necessarily equal. The bulk compositions of both GEMS (in Fig. 6a & i) are given in Table 2.

An example of a GEMS grain that is both thermally altered and contaminated with minor and trace terrestrial contaminants is shown in Fig. 7. There is no rim; however, S, Fe, and Ni are partially segregated, and Mg is segregated from Al and Si and concentrated towards the grain surface. Although less obvious due to its lower abundance (~1.5 at.%), the distribution of Ca is similar to that of Mg. In addition to elements typically found in GEMS, minor (<0.5 at.%) F, P, Cl, Zr, Sn, and Pb are detected using EDX or EELS (Fig. 7j–k) (see Supplementary Material, Fig. S4). The Zr, Sn, and Pb detections are likely due to secondary X-ray fluorescence from components in the microscope electron column. An example of silicone oil contamination, used to collect most IDPs during stratospheric aircraft flights, is shown in Fig. 8.

A thin section of U217B19 was analyzed for H, C, and N isotopes using a Cameca NanoSIMS 50. The purpose of these measurements was to identify isotopically anomalous regions of the grain compared to surrounding material. We consider three dif-

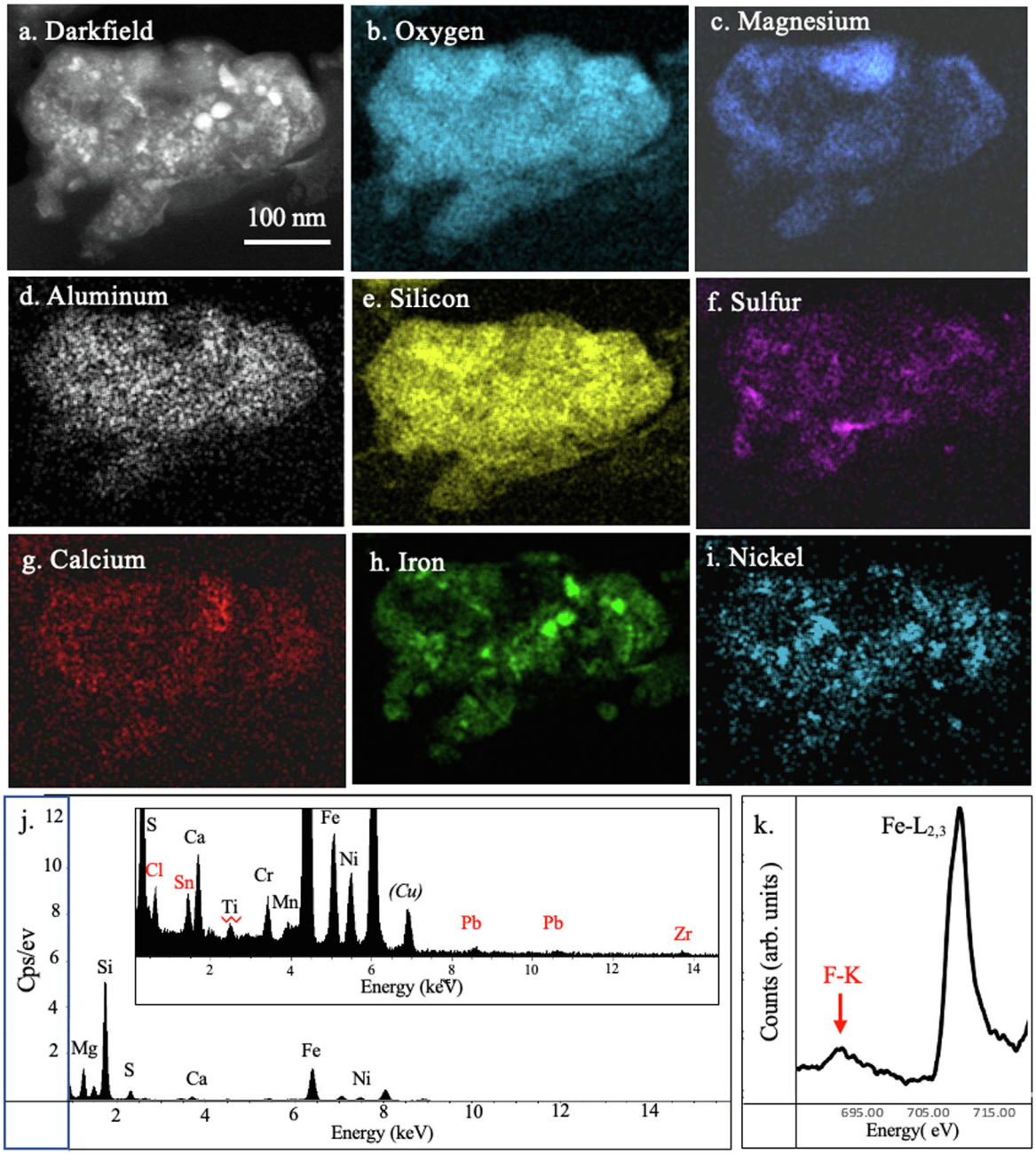

Fig. 7. Thermally altered and contaminated GEMS in U2011 B10. (a) Darkfield image and (b–j) corresponding EDX spectrum images showing the spatial distributions of O, Mg, Al, Si, S, Ca, Fe, and Ni. (j) Bulk EDX spectrum from the grain. The inset is a magnified region of the EDX spectrum showing terrestrial Cl and Sn and Pb artifacts. (k) EELS F-K and Fe-$L_{2,3}$ core scattering edges.

ferent areas of the sample. In the first area, two adjacent ~300 nm "hotspots" with ^{15}N enrichments were found. We calculated the $\delta^{15}N$ value for these two hotspots relative to the bulk particle by defining regions of interest (ROIs) for each hotspot and for the entire particle excluding the hotspots. We calculated the uncertainty in $\delta^{15}N$ values for these hotspots by the bootstrap method. We resampled the pixels, allowing repeats, for the total number of pixels in each hotspot (106 and 115 pixels) and recalculated the $^{15}N/^{14}N$ ratio for each hotspot. We did the same for the entire particle excluding the hotspots (21,876 pixels), and then recalculated $\delta^{15}N$ values for the two hotspots relative to the whole particle. We calculated 100,000 bootstrap replicates for each hotspot $\delta^{15}N$ and then calculated the standard deviation of the two distributions. Our 2σ error of $\delta^{15}N$ is assumed to be twice the standard deviation of the bootstrap distribution. This uncertainty estimate will account for both statistical uncertainty and systematic variations within the ROIs. The first hotspot (on the left in Fig. 9a) is measured to be: $\delta^{15}N$ = 209 ± 53‰ (2σ); the second hotspot (on the right in Fig. 9a) is measured to be: $\delta^{15}N$ = 238 ± 51‰ (2σ).

Both hotspots are carbon-rich, and by comparing to darkfield (HAADF) images, appear to be nanoglobules. (See also Fig. S3.) The lower region of the section, outlined in red, contains pixels with high C/Si (organic carbon-rich regions) and $\delta^{15}N$ that is 39 ± 8‰ (2σ) lower than the upper region of the section with low C/Si (GEMS-rich regions). (The $\delta^{15}N$ difference was calculated with the same bootstrap method used for the hotspots, described above.) The lower values of $\delta^{15}N$ in the carbon-rich region of U217B19, on the lower right of the particle, are shown in Fig. 9c (darker blue).

Table 2
Quantified element abundances of GEMS, sub-regions of GEMS and equilibrated aggregates. Net counts are included solely to demonstrate counting statistics.

	Mg	Al	Si	S	Ca	Ti	Cr	Mn	Fe	Ni
Fig. 2**d W7027 8D, GEMS**										
Net counts	47,414	10,920	139,976	35,279	2570	524	2038	2194	126,895	9883
[wt.%]	10.7	2.6	32.6	8.4	0.8	0.2	0.7	0.8	39.9	3.4
[at.%]	15.8	3.5	41.8	9.4	0.7	0.1	0.5	0.5	25.7	2.1
Rel. error in % (1 Sigma)	3.3	4.1	0.3	3.3	6.9	20.7	7.5	7.0	3.1	3.9
Fig. 2**D W7027 8D, EA**										
Net counts	145,553	21,370	301,897	99,146	11,265	1026	4035	4380	165,520	8052
[wt.%]	17.0	2.6	36.5	12.3	1.5	0.2	0.7	0.8	27.0	1.4
[at.%]	22.9	3.2	42.5	12.5	1.2	0.1	0.4	0.5	15.8	0.8
Rel. error in % (1 Sigma)	3.2	4.0	0.3	3.2	4.8	19.5	7.0	6.5	3.1	5.0
Fig. 3 **LT29, GEMS**										
Net counts	5182	1484	14,431	2608	431	78	256	188	7254	509
[wt.%]	14.4	4.3	41.1	7.6	1.4	0.3	1.0	0.8	27.1	2.1
[at.%]	19.4	5.3	48.1	7.7	1.1	0.2	0.6	0.5	15.9	1.2
Rel. error in % (1 Sigma)	3.5	4.6	0.9	3.9	7.8	20.4	9.4	11.1	3.3	6.8
Fig. 5 **U2011 B10, GEMS**										
Net counts	1238	380	4100	1545	179	33	74	0	3942	219
[wt.%]	9.2	3.0	31.3	12.0	1.5	0.3	0.8	0.0	39.5	2.4
[norm. at.%]	13.6	4.0	40.0	13.4	1.3	0.2	0.5	0.0	25.4	1.5
Rel. error in % (1 Sigma)	4.4	6.8	1.7	4.2	10.2	25.3	15.2	0.0	3.5	8.9
Fig. 6**a, LT29, GEMS interior**										
Net counts	110,560	13,440	161,844	8139	4910	941	3473	3725	69,027	3602
[wt.%]	26.7	3.4	40.2	2.1	1.3	0.3	1.0	1.2	22.5	1.3
[at.%]	34.1	3.9	44.3	2.0	1.0	0.2	0.6	0.7	12.5	0.7
Rel. error in % (1 Sigma)	3.1	3.9	0.3	4.4	5.2	12.7	5.9	5.6	3.1	5.4
Fig. 6**a LT29, GEMS rim**										
Net counts	16,757	1131	28,306	1809	2063	721	1181	5942	168,681	2153
[wt.%]	5.7	0.4	9.9	0.7	0.9	0.3	0.6	2.7	77.7	1.1
[at.%]	11.1	0.7	16.7	1.0	1.1	0.3	0.5	2.3	65.5	0.9
Rel. error in % (1 Sigma)	3.5	10.3	0.9	7.4	6.5	12.4	8.6	4.2	3.0	6.1
Fig. 6**i, LT29, bulk GEMS**										
Net counts	272,969	37,369	514,412	34,732	23,395	3706	10,761	22,617	543,631	19,272
[wt.%]	15.9	2.3	30.8	2.1	1.5	0.3	0.9	1.7	42.7	1.7
[at.%]	23.5	3.1	39.3	2.4	1.4	0.2	0.6	1.1	27.4	1.0
Rel. error in % (1 Sigma)	3.2	4.1	0.2	4.2	4.7	12.1	6.0	4.5	3.1	4.6
Fig. 7**, U2011 B10, GEMS**										
Net counts	20,692	9700	91,607	7814	3349	705	2043	820	42,301	3987
[wt.%]	10.1	5.0	46.0	4.0	1.8	0.5	1.2	0.6	27.8	2.9
[at.%]	13.9	6.2	54.6	4.1	1.5	0.3	0.8	0.4	16.6	1.6
Rel. error in % (1 Sigma)	3.3	3.7	0.4	3.8	4.9	10.2	5.9	8.8	3.1	4.3
Fig. 8 **LT29, GEMS**										
Net counts	48,761	8414	102,456	34,132	4107	2674	2751	78,564	534	4385
[wt.%]	15.1	2.8	32.6	11.0	1.4	1.0	1.1	32.7	0.2	2.0
[at.%]	21.2	3.5	39.6	11.8	1.2	0.7	0.7	20.0	0.2	1.2
Rel. error in % (1 Sigma)	3.2	4.1	0.4	3.3	5.2	6.1	5.9	3.1	16.6	4.7
Fig. 8**, LT29, metal inclusion**										
Net counts	85	22	1012	112	0	0	2	237	6955	1523
[wt.%]	0.6	0.2	7.9	0.9	0.0	0.0	0.0	2.4	70.9	17.1
[at.%]	1.4	0.3	14.4	1.5	0.0	0.0	0.0	2.2	65.2	14.9
Rel. error in % (1 Sigma)	15.1	35.6	3.5	12.6	0.0	0.0	188.2	8.6	3.3	4.2

Oxygen isotopes were measured in U217B19 by NanoSIMS to search for presolar grains. We define an isotopically anomalous region to be an area >100 nm across that is >5σ different from the surrounding material. No such regions were identified. Using standards measured prior to the sample, the bulk oxygen isotopic composition of the whole particle hints at terrestrial rather than solar composition for the bulk particle, although the accuracy of the measurement may be poor due to insufficient standardization. Using the same definition, no anomalous regions in the D/H or $^{13}C/^{12}C$ isotope ratio images were identified.

4. Discussion

The compositions, mineralogy and petrography of the GEMS we describe are typical of those of the larger population of >100 GEMS described in the literature (Bradley, 1994a,b; Ishii et al., 2008, 2018; Dobrică et al., 2012; Keller and Messenger, 2011; Noguchi et al., 2017). Their approximate sizes, rounded shapes, Fe^0Ni^0 metal and $Fe^{2+}Ni^{2+}$-sulfide inclusions, amorphous Mg-silicate and organic carbon association are assumed to be original (indigenous) properties because of their highly unequilibrated nature. The original bulk compositions of GEMS are expected to be variable, because the relative abundances of inclusions and matrix are variable from one GEMS grain to another. The literature demonstrates that GEMS' bulk average compositions are slightly sub-solar in volatile and moderately volatile elements when ratioed to Si. Although it is not technically feasible to perform combined EDS and EELS spectrum imaging on a statistically significant population of GEMS, our observations illustrate the types of alteration that can impact their element/Si ratios. Below, we discuss the low densities of GEMS and the causes of alteration and implications of sub-solar element/Si ratios reported in the literature. We assess the assump-

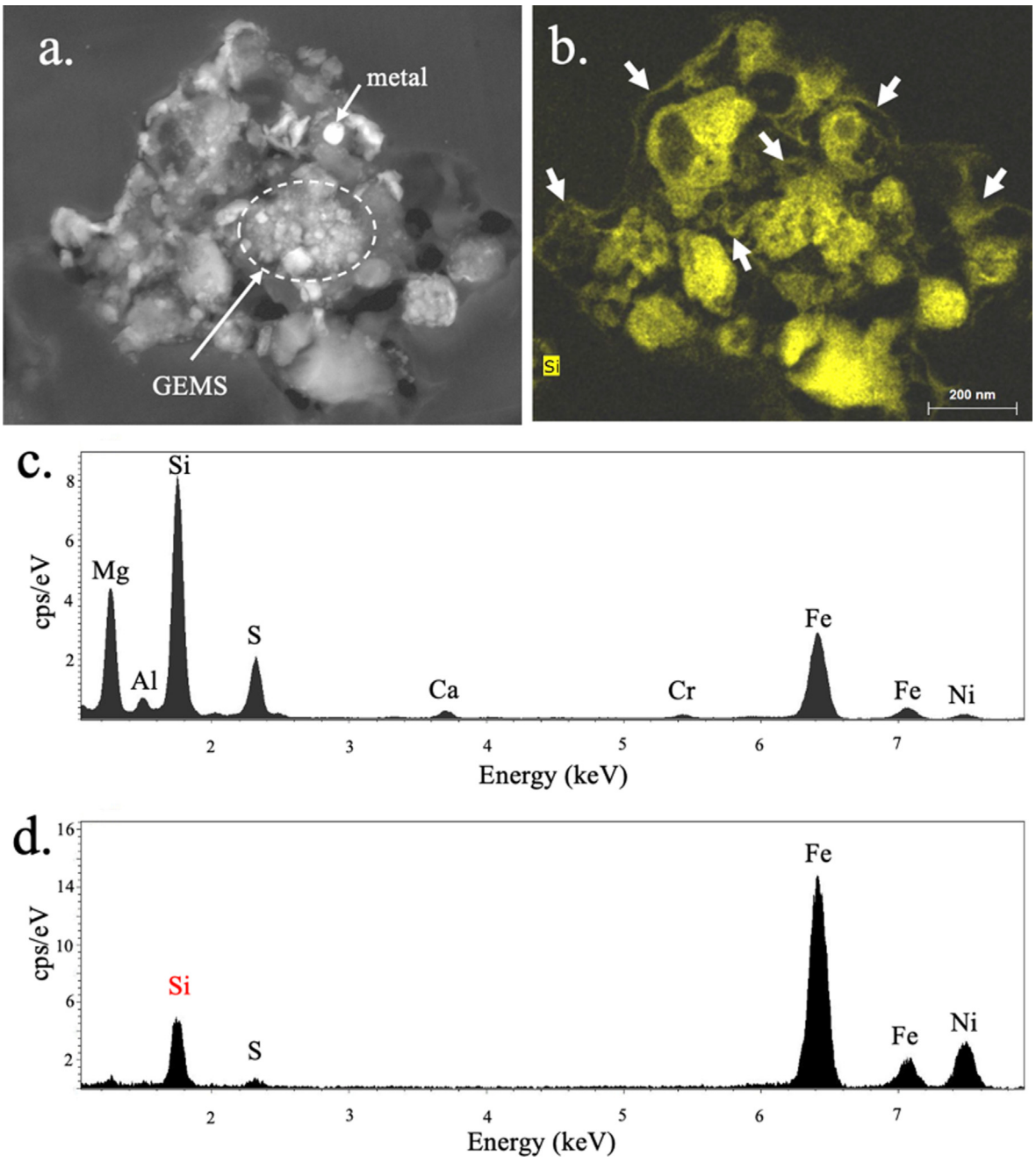

Fig. 8. Silicone oil contamination in GEMS in LT29. (a) Darkfield image and (b) EDX spectrum image showing the distribution of Si. Si-rich halos (arrowed in b) around most grains are retained silicone oil. (c) EDX spectrum from the GEMS in which Si contributions from silicone oil are indistinguishable from indigenous Si, and (d) the nominally Si-free FeNi metal grain (indicated in a). The absence in (d) of other cations typical in silicates indicates that the Si observed at the metal grain is due to retained silicone oil rather than overlapping silicate or GEMS grains.

tion of complementarity of compositions of GEMS and associated crystals within IDPs, and we consider the implications of nitrogen and oxygen isotopic enrichments in GEMS-rich regions. Finally, we examine the prospects for GEMS identification in primitive meteorite matrices.

4.1. Underdense GEMS

Due to less efficient packing of atoms, melt glass atomic densities are typically 90–95% of their corresponding crystals, and GEMS have generally been assumed to be similarly dense. We find that GEMS are significantly underdense with atomic densities ~35–65% of silicate crystal aggregates with very similar average composition (Fig. 2, Table 1). GEMS are thus significantly underdense, far less than the ~90–95% estimate for melt glasses and consistent with differences observed in HAADF contrast (Figs. 1, 2c).

Other measurements support underdense GEMS and provide additional information on the causes of their low densities: Infrared spectra from (GEMS-rich) IDPs do not show a ~10 μm silicate feature characteristic of amorphous silicates. Only the crystalline silicate components are detected, and the ~10 μm feature from individual GEMS is conspicuously weak (Bradley et al., 1992, 1999). Valence band EELS spectra from some GEMS reveal strong surface plasmons, indicative of high densities of dangling bonds

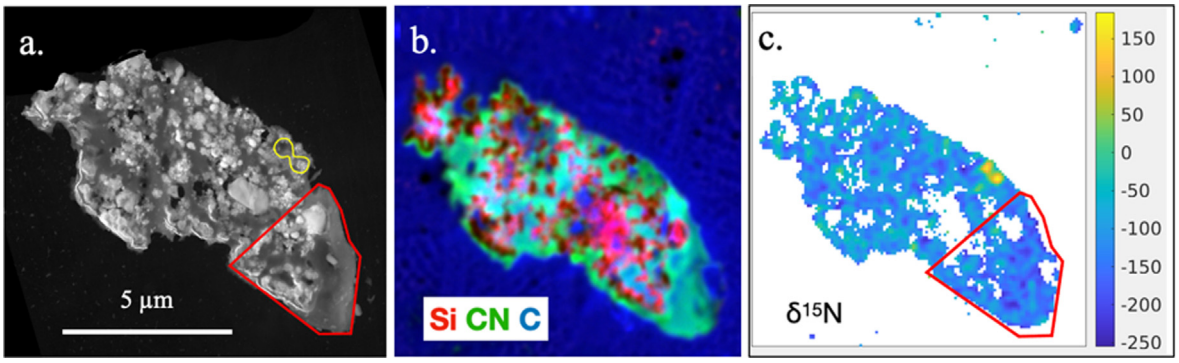

Fig. 9. Distribution of $\delta^{15}N$ in GEMS-rich and carbon-rich regions in U217B19. (a) Darkfield image. Yellow and red outline regions with high $\delta^{15}N$ and low $\delta^{15}N$, respectively, as shown in (c). (b) NanoSIMS scanning ion RGB image of Si (red), CN (green), and C (blue). Each element is normalized to the secondary electron image (to account for variation in ion emission), and each element histogram is normalized using Matlab's imadjust function. (c) $\delta^{15}N$ image showing two $\delta^{15}N$ hotspots of +209 ± 53‰ (left yellow outline in (a)) and +238 ± 51‰ (right yellow outline in (a)), and the carbon-rich region at lower-right with lower $\delta^{15}N$. The carbon-rich regions of U217B19 are 39 ± 8‰ lower in $\delta^{15}N$, on average, than the GEMS-rich areas in the upper region of the IDP. Pixels with statistical noise above a threshold are displayed as white.

and nanoporosity similar to valence band spectra from H^+ and He^+ irradiated surfaces (Hojou et al., 1998; Bradley, 2014). This nanoporosity and resulting low density may be a result of space weathering (discussed below in Section 4.3.3), specifically irradiation and sputtering prior to incorporation into small parent bodies (Bradley, 1994a; Jäger et al., 2016). Most GEMS are stoichiometrically enriched in oxygen that has been shown to be most likely due to hydroxyl, also consistent with irradiation exposure (Bradley, 1994a; Bradley et al., 2014; Daly et al., 2021). While ion implantation in GEMS is likely, gaseous species in amorphous silicate and carbonaceous components of GEMS may not be retained due to their more open structures. However, hydroxyl and/or water has been detected in vesicles in crystalline components associated with GEMS in IDPs (Bradley et al., 2014). Finally, the presence of organic carbon not only around, but also within, GEMS also reduces their overall densities (Dai et al., 2002; Ishii et al., 2018).

The low densities of GEMS have direct (negative) implications on their survivability in parent bodies that experience any compaction, thermal or aqueous processing. It also has implications for GEMS capacity to take up contamination, in particular silicone oil, with direct impact on measured element/Si ratios. GEMS' low densities also contribute to selection bias for analyses since their low densities result in low imaging contrast; more altered GEMS that have experienced sintering or have absorbed silicone oil, increasing their density, are more likely to be selected for analysis. These implications are discussed further in Section 4.3.

4.2. Evidence for alteration of GEMS

Although GEMS clearly formed as highly unequilibrated materials, their element distributions (Figs. 3–8) indicate that they have experienced varying degrees of secondary alteration, sometimes obvious, but more often, subtle. Combined EDX and EELS spectrum mapping of some GEMS in IDPs reveals evidence of significant alteration of metal and sulfide inclusions, such as volatile loss and oxidation, but with minimal evidence for alteration of the glassy matrix (e.g., Figs. 3 & 4). Such alteration is subtle and easily overlooked. Other GEMS show more advanced Fe oxidation, evident in oxidation rims on GEMS and inclusions within GEMS, and even elemental segregation (e.g., Fig. 5). GEMS on the surfaces of IDPs were exposed directly to terrestrial oxygen during upper atmospheric entry and developed partial Fe-rich oxide rims on their surfaces (Fig. 6). These have generally been acknowledged as "altered" in prior literature and omitted in compositional analyses of GEMS. They show internal depletions in Mg, Ca, Fe, and Ni in the interior regions behind the rim, and the heavily oxidized Fe-rich rim shows enrichment in those elements, indicating that, while forming, the rim acts to collect mobilized elements. Internal depletions and rim enrichments of Mg, S, Ca, Fe, and Ni relative to Si are common among GEMS. Many GEMS also show evidence of terrestrial contamination, whether from residence in Earth's atmosphere or on its surface, from sample collection, or from sample preparation. Silicon contamination, in particular, is implicated in sub-solar element/Si ratios. Evidence for alteration as it pertains to sub-solar element/Si ratios is discussed in more detail in Section 4.3.1.

4.3. Causes and implications of sub-solar element/Si ratios

In the following, we consider how and where alteration may have occurred and then evaluate the use of composition to assess provenance.

4.3.1. Pulse heating

IDPs are frictionally pulse heated at an altitude of ~90 km for several seconds during atmospheric entry. The duration of the pulse and peak temperature are a function of entry speed and angle, and most IDPs are heated above 500 °C for several seconds (Love and Brownlee, 1991, 1996). Frictional heating during deceleration in a column of oxygen-rich atmosphere causes oxidation of Fe to $Fe^{2+}$and Fe^{3+} (e.g., Figs. 4 & 5), accompanied by thermal mobilization and partial loss of Mg, S, Ca, Fe, and Ni, and an overall reduction in element/Si ratios in GEMS (e.g., Figs. 3, 5–7). Elements trapped in Fe-rich oxide rims that form on the surfaces of GEMS directly exposed to air serve as "witness plates" to the thermal effects of atmospheric entry (Fig. 6). Laboratory heating experiments indicate that sulfide decoration of GEMS surfaces (e.g., Fig. 3), rather resulting from exposure in the solar nebula (Matsuno et al., 2022), may instead be a result of recent pulse heating during atmospheric entry Since GEMS with rims, such as in Fig. 6, are observed in solar-flare-track-rich IDPs, and tracks are erased at ~650 °C, changes in composition (element/Si ratios) occurr at much lower temperatures than has been assumed (Bradley et al., 1984).

4.3.2. Contamination

While resident in the terrestrial environment, IDPs and GEMS become contaminated. We observed minor/trace (typically <1.0 wt%) levels of F, P, Cl, Zr, Sn, and Pb by EDX and EELS (Figs. 7 and S4). Solvent residues, embedding media, and stratospheric contamination, possibly including anthropogenic chlorofluorocarbons, are likely sources of F, P, Cl, and Br (Rost et al., 1999; Stephan, 2001; Flynn et al., 2003). Zr, Sn, and Pb are known analyt-

ical artifacts in the TEM (Fig. 7). Minor/trace P commonly detected in GEMS-rich IDPs is potentially significant, due to its detection in comets and relevance to astrobiology, but contamination from atmospheric aerosols is also likely (see Supplementary Material Fig. S4) (Shi et al., 2019; Altwegg, 2022).

Most IDPs have been collected by impact onto silicone-oil-coated "flags" mounted on aircraft wing pylons, and silicone oil is the principal, though highly variable, terrestrial contaminant of IDPs and GEMS. Silicone oil is an insidious contaminant because, although it is readily distinguished on surfaces of metal and sulfide grains that contain no Si, it can be indistinguishable in and on (Si-rich) GEMS due to their underdense glassy matrix (Fig. 8). One complication of silicone oil is that the degree of its removal likely depends on particle properties like porosity, and different protocols have been used to remove it. Fraundorf (1981) cautioned that excess Si should be viewed with suspicion, Flynn et al. (1978) found that removal of silicone oil is incomplete, and Rietmeijer (1987) described silicone oil as a "persistent contaminant". Rost et al. (1999) found that surface-bound silicone oil on six out of thirteen IDPs collected in the stratosphere was severe enough to preclude reliable surface elemental analysis. Schramm et al. (1989) and Thomas et al. (1993) estimate that as much as 10–12 wt% of the Si in IDPs may be retained silicone oil. GEMS' low density may enable enhanced uptake of silicone oil and other terrestrial contamination (discussed below in Section 4.4). Sub-solar bulk GEMS element/Si ratios reported in the literature may be a result of excess Si from silicone oil contamination, in some cases. Without knowing the original element abundances in GEMS, it is not possible to quantify the impact of silicone oil on the measured element/Si ratios, although this study that includes an IDP (U2011 B10, see Table 2 entries for Fig. 5 and Fig. 7) collected in (silicone-oil-free) polyurethane shows that silicone oil is not solely responsible for low element/Si ratios in GEMS.

We note that GEMS in chondritic porous and ultracarbonaceous micrometeorites (MMs) may be expected, on average, to be less depleted in element/Si than stratospheric IDPs because they are not collected in silicone oil and, thus, are not Si-enriched. Since MMs are typically 5–10 × larger than IDPs, however, they generally experience stronger heating during atmospheric entry (e.g., Genge et al., 2020) and resultant oxidation and element/Si depletions. In addition, MMs collected from snow or meltwater suffer minor leaching to more severe aqueous alteration that also impacts element/Si ratios (e.g., Noguchi et al., 2017). These alterations notwithstanding, the least-altered MMs may contain GEMS with more pristine element/Si compositions since they are not Si-contaminated.

4.3.3. Space weathering

The low densities of GEMS determined using EDX (Fig. 2) are consistent with nanoporosity that may result from irradiation and sputtering during space weathering, as mentioned in Section 4.1. Sputtering, combined with redeposition on grain surfaces during residence in cold (<50 K) environments, precludes atomic rearrangement that would lead to denser material. Significant alteration may also have occurred in conjunction with photolytic deposition of organic carbon during the initial stages of GEMS accretion in the extreme outer solar nebula, presolar molecular cloud, and the ISM (Noguchi et al., 2017; Ishii et al., 2018). Following release into the interplanetary space, the surfaces of some GEMS are also exposed to solar wind for timescales on the order of 10–1000 ka (Bradley et al., 1984; Keller and Flynn, 2022). Laboratory experiments confirm that irradiation causes reductions in several element/Si ratios in minerals (Bradley, 1994a; Noguchi et al., 2011; Carrez et al., 2002).

4.3.4. Parent body alteration

Element abundances may be reduced and/or redistributed (e.g., Figs. 4 & 5) by limited aqueous leaching while GEMS are sequestered in small, ice-rich parent bodies for ~4.6 Ga. Depletions in Mg/Si and S/Si and enrichment in Fe^{3+} in GEMS have been interpreted as evidence of oxidation and leaching within comets (Yabuta et al., 2017; Noguchi et al., 2017). Laboratory experiments show that GEMS are highly susceptible to rapid aqueous alteration at temperatures as low as 433 K (160 °C), Nakamura-Messenger et al., 2011). Terrestrial amorphous silicates (e.g., obsidian) are readily leached with oxidation of Fe and a decrease in density and element/Si ratios under both experimental and natural weathering conditions, including during long-term (~1 ka) storage in ice (Koenderink et al., 2000; Vesavage et al., 2015). Similar alteration conditions may exist in small, ice-rich asteroids and comets (Harju et al., 2014; Yabuta et al. 2017; Noguchi et al., 2017; Rietmeijer, 2018). The low density of GEMS (Fig. 2, Table 1) also indicates that they would be more highly susceptible to parent body alteration.

4.3.5. Limitations of composition in determining provenance

Although it is not possible to quantitatively determine which of the above alteration processes, if any, are dominant, the presence of oxidized rims on GEMS in IDPs that retain solar flare tracks shows that thermal alteration during atmospheric entry occurs at a much lower temperature and is more extensive than has been assumed. In addition, silicone oil contamination lowers element/Si ratios; its retention in IDPs varies from severe to minimal depending on properties like size, porosity, carbon content, solvent washing protocols, the efficacy of removal using solvents, and polymerization in samples previously exposed to an electron beam. Uncertainty about the composition of interstellar dust relative to solar abundances further complicates reliance on element/Si ratios (Voshchinnikov and Henning, 2010; Zhukovska et al., 2018: Draine and Hensley, 2021; Hensley and Draine, 2021). Regardless of how GEMS are compositionally altered, element/Si ratios are insufficient to establish their provenance.

4.4. Assessing the assumption of complementary compositions of GEMS and crystals

The hot origin hypothesis for GEMS formation argues that, since CP IDPs have approximately solar bulk compositions and GEMS have sub-solar element/Si compositions, then the accompanying crystals must have complementary super-solar element/Si compositions and a single solar reservoir was the origin of both (Keller and Messenger, 2011). We note first that the average composition of GEMS grains can, alternatively, be considered to be Si-enriched (~1.5 × solar) and approximately solar in other major and minor elements. This interpretation is consistent with observations of excess Si observed around and in CP IDPs from residual silicone oil contamination. A fundamental property of GEMS is that they are underdense, ~35–65% of crystalline silicates, and this low density and nano-porosity may enhance their uptake of terrestrial contamination, especially silicone oil. These considerations indicate that GEMS' measured sub-solar element/Si compositions are not entirely indigenous and thus suspect in arguments regarding GEMS origin as discussed in Section 4.3.5. Second, complementarity between GEMS and crystals has not been rigorously demonstrated within CP IDPs. Different populations of CP IDPs were analyzed for the bulk IDP element/Si ratios (Schramm et al., 1989) and for the GEMS element/Si ratios (Keller & Messenger, 2011). As a result, different levels of silicone oil contamination may have been retained in the two sets of IDPs. Third, CP IDPs have historically been considered "chondritic" if their compositions fall within a factor of ~2–3 × solar, a remarkably wide window of compositions that can readily accommodate sub- and super-solar element/Si ratios

of components without requiring complementarity between them. Furthermore, the contribution of GEMS to whole IDP compositions must be weighted not only by their (variable) volume fraction in IDPs, but also by their atomic densities, which are significantly lower than has been historically assumed. Because GEMS are underdense, they contribute less to the bulk CP IDP composition than their volume in TEM cross-sections would suggest. Finally, there is also probable selection bias in historical GEMS analyses: Altered GEMS that have experienced densification of their amorphous silicate matrix show higher contrast in TEM imaging, drawing the eye. Pristine GEMS, lower in density, are less visible and less likely to be selected for analysis due to their lower contrast. The impacts on GEMS element/Si ratios from atmospheric entry, terrestrial contaminants (predominantly added Si from silicone oil contamination), and potential parent body and space weathering alteration processes, combined with GEMS' low densities and the likely over-selection of more altered GEMS in analyses, all serve to undermine any assumption of complementarity between GEMS and crystal components in CP IDPs.

4.5. Isotope anomalies

Enriched $^{15}N/^{14}N$ ratios in the organic matter in chondritic meteorites are interpreted as resulting from ion-molecule reactions in cold, interstellar molecular clouds or outer regions of protoplanetary disks (Messenger, 2000; Ishii et al., 2018), although, as Chakraborty et al. (2014) pointed out, these ion–molecule reactions should also produce large $^{13}C/^{12}C$ and D/H fractionations, which are not always found accompanying the $^{15}N/^{14}N$ enrichments. We observe $^{15}N/^{14}N$ enrichment in U217B19 in GEMS-rich and in organic carbon-rich regions (Figs. 9 & S3), suggesting a presolar origin for the organics. The higher $^{15}N/^{14}N$ enrichment in the GEMS-rich regions further indicates a difference in the organic carbon in the two types of regions. The significance of $^{15}N/^{14}N$ enrichment in U217B19 is that it has been shown to be carried by a higher-density organic carbon in nanoglobules and mantles on GEMS surfaces (Ishii et al., 2018, Supplementary Material). The higher density presumably reflects higher aromatic (PAH) content, because the most aromatic-rich nanoglobules in insoluble organic matter in some chondritic meteorites are also carriers of the largest ^{15}N isotope enrichments (De Gregorio et al., 2013). Furthermore, GEMS-rich IDPs are among the materials with the highest abundance of isotopically anomalous presolar components of any known meteoritic material (Floss and Haenecour, 2016). Highly anomalous nonsolar oxygen isotope ratios measured in some GEMS indicate incorporation of presolar stardust (Messenger et al., 2003; Floss et al., 2006; Busemann et al., 2009).

Within experimental error, however, the O isotopic compositions of most GEMS trend towards the terrestrial value (Keller and Messenger, 2011). This does not imply a terrestrial or even Solar System origin of the oxygen in GEMS. *Bona fide* stardust, i.e., circumstellar grains that condensed around evolved stars have isotopic compositions of the stellar material from which they condensed. However, it is expected that the amorphous dust in the ISM experiences isotopic homogenization. Compared to anomalies in circumstellar stardust grains, the ~6% difference in oxygen isotope ratios between terrestrial or meteoritic and solar is rather small (McKeegan et al., 2011) and is hard to detect, at least in samples as small as typical GEMS grains. Nevertheless, it is true that, while some GEMS are indisputably presolar in origin, for most GEMS the oxygen isotopic data reported previously are consistent with terrestrial/meteoritic oxygen but, on average, inconsistent with solar oxygen. The origin of isotopic difference between the Sun and the Earth/meteorite parent bodies is still unknown. One possible explanation is that CO self-shielding in the early Solar System or in its parent molecular cloud has caused a depletion, relative to the Sun, of ^{16}O in regions where the meteorite parent bodies and the Earth eventually formed (Clayton, 2002; Yurimoto and Kuramoto, 2004; Lyons and Young, 2005). In that model, the Solar System evolved from initially isotopically homogeneous, ^{16}O-rich gas and dust, and fractionation from self-shielding occurred later during the formation of solids. However, as Krot et al. (2010) pointed out, no solar-like, ^{16}O -rich primordial dust has yet been discovered, which led to the model that primordial dust and solar nebula gas did not have identical oxygen isotopic composition to start with (Krot et al., 2010). In that model, the ^{16}O-rich composition of amoeboid olivine aggregates and CAIs from primitive meteorites is explained by their condensation from a gas with close-to-solar composition and a very low dust/gas ratio. Other meteorite components, as well as the Earth, would instead reflect the oxygen isotopic composition of the primordial dust. In that scenario, it is expected that most interstellar solids (excepting surviving circumstellar stardust) are more Earth-like than solar in their oxygen isotopic composition, as seems to be the case for GEMS. As long as the O isotope dichotomy between the Sun and terrestrial bodies is not fully understood, especially while it remains unknown if this dichotomy was inherited from the protosolar molecular cloud (e.g., Krot, 2019), O isotopes cannot enable us to distinguish between a single interstellar provenance for all GEMS or two different provenances with one clearly interstellar. Nevertheless, iron oxidation in the atmosphere and contamination with silicone oil, during collection are two potential sources of added terrestrial oxygen in GEMS, which could dilute any indigenous isotopic anomaly.

4.6. "GEMS-like" matrix in meteorites

It has been suggested that "GEMS-like" materials in the least altered meteorites that are texturally and compositionally similar to GEMS in IDPs, are compacted and minimally altered GEMS (Leroux et al., 2015, Suttle et al., 2017; Nittler et al., 2019). Like GEMS in IDPs, this material consists of S, Fe, and Ni-rich inclusions in amorphous Mg-Fe silicate matrix. However, the inclusions in GEMS-like material are mostly FeNi sulfides, carbides and oxides, and (FeNi) metal inclusions are conspicuously rare or absent (Bradley, 2020; Villalon et al., 2021; Ohtaki et al., 2021). Although it is possible that metal inclusions were selectively altered and destroyed under conditions of mild parent body alteration, this study of GEMS alteration in IDPs indicates that it is the sulfide inclusions rather than metal inclusions that are more susceptible to alteration. The amorphous silicate matrix in GEMS-like material is also more Fe-rich than in GEMS in IDPs (e.g., Ohtaki et al., 2021), which may be more consistent with formation of GEMS-like material via rapid condensation from the gas phase under non-equilibrium conditions prior to accretion in meteorite parent bodies. The anomalously low densities of GEMS may explain why they have yet to be rigorously identified in even the least altered meteorites. They may not survive in recognizable form in bodies that experienced even weak or gentle compaction, thermal metamorphism, or aqueous alteration.

5. Conclusions

We have reviewed historical hypotheses for the provenance of GEMS and further investigated their elemental and isotopic compositions and densities using a combination of electron microscopy and secondary ion mass spectrometry. Like all meteoritic materials that have experienced some alteration, despite terrestrial alteration that perturbs element/Si ratios, indigenous mineralogy and some isotopic compositions of GEMS are discernable and reflective of their provenance.

We conclude the following:

1. GEMS are systematically and significantly lower in density (estimated at ~35–65%) than crystalline constituents with similar

compositions. Rather than a complementary compositional relationship between (low density) GEMS and the crystalline components of CP IDPs, it is the (higher density) crystalline components that dominate the solar compositions of CP IDPs.
2. The chemical compositions of GEMS, as collected and characterized, are not indigenous (original) because they have been perturbed by secondary alteration, most recently upon entry into the terrestrial environment. The wide (<10×) variation in individual element/Si ratios among the GEMS population thus reflect both their original composition range and variable extent of alteration, that may continue post-collection. Consequently, systematic depletions in their element/Si ratios are insufficient to inform about their provenance.
3. The nitrogen isotopic composition of organic carbon within and mantling GEMS surfaces clearly implicates a low-temperature (<50 K) provenance. The coexistence of (S-free) FeNi metal and (S-rich) FeNi sulfide nano-inclusions, as well as the immiscibility of sulfides in silicates at any temperature, also implicate a low-temperature accretional provenance.
4. According to models that primordial dust and solar nebula gas did not have identical oxygen isotopic composition at the collapse of the presolar molecular cloud (e.g., Krot et al., 2010), oxygen isotopic compositions among the GEMS population are consistent with a presolar interstellar provenance.
5. Collectively the properties of GEMS are unique among known meteoritic materials and consistent with dust in dense molecular clouds and diffuse ISM environments. We favor the provenance scenario proposed by Ishii et al. (2018): GEMS inorganic constituents and condensing organic carbon co-aggregated in the presolar molecular cloud and outer regions of the protoplanetary disk. As such, some GEMS are, and all GEMS may be, examples of the original bricks and mortar of the Solar System that have been sequestered in small icy bodies beyond the giant planets for the past ~4.6 Ga.

Declaration of Competing Interest

The authors declare that they have no known competing financial interests or personal relationships that could have appeared to influence the work reported in this paper.

Acknowledgements

We acknowledge the life-long contributions of Christine Floss (Washington University in St. Louis), who collected the initial isotopic composition data on the IDP U217B19 thin section but, unfortunately, passed away prior to publication of this work. We thank Jeffrey Cuzzi, Bruce Draine and Aigen Lee for useful discussions. We also thank Andrew Thron at Ametek for MLLS analysis training and support. This manuscript benefited greatly from helpful comments and suggestions from Cecile Engrand and two anonymous reviewers. H.A.I. acknowledges funding by NASA's Laboratory Analysis of Returned Samples and Emerging Worlds Programs (grants NNX14AH86G and NNX16AK41G). R.O. acknowledges funding by NASA's Emerging Worlds Program (grant NNX14AG25G). T.S. was funded by NASA (grants 80NSSC20K0869 and 80NSSC21K0374). Work at the Molecular Foundry was supported by the Office of Science, Office of Basic Energy Sciences, of the U.S. Department of Energy under Contract No. DE-AC02-05CH11231.

Appendix A. Supplementary material

Supplementary material to this article can be found online at https://doi.org/10.1016/j.gca.2022.06.036.

References

Altobelli, N., Postberg, F., Fiege, K., Trieloff, M., Kimura, H., Sterken, V.J., Hsu, H.-W., Hillier, J., Khawaja, N., Moragas-Klostermeyer, G., Blum, J., Burton, M., Srama, R., Kempf, S., Gruen, E., 2016. Flux and composition of interstellar dust at Saturn from Cassini's Cosmic Dust Analyzer. Science 352, 312–318.
Altwegg, K., 2022. Cometary chemistry. Phys. Today 75, 34–41.
Bradley, J.P., 1984. Analysis of interplanetary dust thin sections. Geochim. et Cosmochim. Acta 52, 889–900.
Bradley, J.P., 1994a. Chemically anomalous, preaccretionally irradiated grains in interplanetary dust from comets. Science 265, 925–929.
Bradley, J.P., 1994b. Nanometer-scale mineralogy and petrography of fine-grained aggregates in anhydrous interplanetary dust particles. Geochim. Cosmochim. Acta 58, 2123–2134.
Bradley, J.P., 2014. Early solar nebula grains – interplanetary dust particles. In: Davis, A.M. (Ed.), Meteorites and Cosmochemical Processes, vol. 1, Treatise on Geochemistry, second ed. (Exec. Eds. H. D. Holland and K. K. Turekian). Oxford: Elsevier; pp. 287–308.
Bradley, J.P., Humecki, H.J., Germani, M.S., 1992. Combined infrared and analytical electron microscope studies of interplanetary dust particles. Astrophys. J. 394, 643–651.
Bradley, J.P., Ishii, H.A., Gillis-Davis, J.J., Ciston, J., Nielsen, M.H., Bechtel, H.A., Martin, M.C., 2014. Detection of solar wind-produced water in irradiated rims on silicate minerals. Proc. Nat. Acad. Sci. 111, 1732–1735.
Bradley, J.P., 2020. GEMS and the devil in their details. Nat. Aston. 3, 602–605.
Bradley, J.P., Brownlee, D.E., Fraundorf, P., 1984. Discovery of nuclear tracks in interplanetary dust. Science 226, 1432–1434.
Bradley, J.P., Ishii, H.A., 2008. Comment on "The shape and composition of interstellar silicate grains". Astron. Astrophys. 486, 781–784.
Bradley, J.P., Keller, L.P., Snow, T.S., Hanner, M.S., Flynn, G.J., Gezo, J.C., Clemett, S.J., Brownlee, D.E., Bowey, J.E., 1999. An infrared spectral match between GEMS and interstellar grains. Science 285, 1716–1718.
Busemann, H., Ngyuen, A.N., Cody, G.D., Hoppe, P., Klicoyne, A.L.D., Stroud, R.M., 2009. Ultra-primitive interplanetary dust particles from the comet 26P/Grigg-Skjellerup dust stream collection. Earth Planet. Sci. Lett. 288, 44–57.
Carrez, P., Demyk, K., Cordier, P., Gengembre, L., Grimblot, J., d'Hendecourt, L., Jones, A.P., Leroux, H., 2002. Low-energy helium ion irradiation-induced amorphization and chemical changes in olivine: Insights for silicate dust evolution in the interstellar medium. Meteorit. Planet. Sci. 37, 1599–1614.
Chakraborty, S., Muskatel, B.H., Jackson, T.L., Ahmed, M., Levine, R.D., Thiemens, M. H., 2014. Massive isotope effect in vacuum UV photodissociation of N_2 and implications for meteorite data. Proc. Natl. Acad. Sci. 111, 14704–14709.
Clayton, R.N., 2002. Self-shielding in the solar nebula. Nature 415, 860–861.
Dai, Z.R., Bradley, J.P., 2001. Iron-nickel sulfides in anhydrous interplanetary dust particles. Geochim. Cosmochim. Acta 63, 3601–3612.
Dai, Z.R., Joswiak, D.J., Bradley, J.P., Joswiak, D.J., Brownlee, D.E., Hill, H.G.M., Genge, M.J., 2002. Possible in situ formation of nano-diamonds in the early solar system. Nature 418, 157–159.
Daly, L., Lee, M.R., Hallis, L.J., Ishii, H.A., et al., 2021. Solar contributions to Earth's oceans. Nat. Astron. 5, 1275–1285.
Dartois, E., Muñoz-Caro, G.M., 2007. Carbonaceous dust grains in luminous infrared galaxies. Spitzer/IRS reveals a-C: H as an abundant and ubiquitous ISM component. A & A 476, 1235–1242.
De Gregorio, B.T., Stroud, R.M., Nittler, L.R., Alexander, C.M.O'D., Bassim, N.D., Cody, G.D., Kilcoyne, A.L.D., Sandford, S.A., Milam, S.N., Nuevo, M., Zega, T., 2013. Isotopic and chemical variation of organic nanoglobules in primitive meteorites. Meteorit. Planet. Sci. 48, 904–928.
Dobrică, E., Engrand, C., Leroux, H., Rouzaud, J.-N., Duprat, J., 2012. Transmission electron microscopy of the CONCORDIA UltraCarbonaceous Antarctic MicroMeteorites (UCAMMs): Mineralogical properties. Geochim. Cosmochim. Acta 76, 68–82.
Draine, B.T., 2009. Interstellar dust models and evolutionary implications. In: Henning, Th., Gruen, E., Steinacker, J. (Eds.), Cosmic Dust Near and Far. ASP Conference Series, vol. 414, pp. 453–472.
Draine, B.T., 2011. Astronomical models of PAHs and dust. In: Joblin, C., Tielens, A.G. G.M. (Eds.), PAHs and the Universe, EAS Publications Series, vol. 46, pp. 29–42.
Draine, B.T., Hensley, B.S., 2021. The dielectric function of "Astrodust" and predictions for polarization in the 3.4 and 10 μm features. Astrophys. J. 909, 94–115.
Floss, C., Haenecour, P., 2016. Presolar silicate grains: abundances, isotopic and elemental compositions, and the effects of secondary processing. Geochem. J. 50, 3–25.
Floss, C., Stadermann, F.J., Bradley, J.P., Dai, Z.R., Bajt, S., Graham, G., Lea, A.S., 2006. Identification of isotopically primitive interplanetary dust particles: a NanoSIMS isotopic imaging study. Geochim. Cosmochim. Acta 70, 2371–2399.
Flynn, G.J., Fraundorf, P., Shirck, J., Walker, R.M., 1978. Chemical and structural studies of Brownlee particles. In: Proc. Lunar Planet. Sci. Conf. 9th, pp. 1187–1208.
Flynn, G.J., Keller, L.P., Wirick, S., Jacobsen, C., Sutton, S.R., 2003. Analysis of interplanetary dust particles by soft and hard X-ray microscopy. J. de Physique IV (Proc.) 104, 367–372.
Fraundorf, P., 1981. Interplanetary dust in the transmission electron microscope: diverse materials from the early solar system. Geochim. Cosmochim. Acta 45, 915–943.

Genge, M.J., van Ginneken, M., Suttle, M.D., 2020. Micrometeorites: Insights into the flux, sources and atmospheric entry of dust at Earth. Planet. Space Sci. 187, 104900.
Goodman, A.A., Whittet, D.C.B., 1995. A point in favor of the superparamagnetic grain hypothesis. Astrophys. J. Lett. 455, L181–L184.
Harju, E.R., Rubin, A.E., Ahn, I., Choi, B.-G., Ziegler, K., Wasson, J.T., 2014. Progressive aqueous alteration of CR carbonaceous chondrites. Geochim. Cosmochim. Acta 139, 267–292.
Hanner, M.S., Brooke, T.Y., Tokunaga, A.T., 1998. 8–13 micron spectroscopy of young stars. Astrophys. J. 502, 871–882.
Hensley, B.S., Draine, B.T., 2021. Observational constraints on the physical properties of interstellar dust in the post-Planck era. Astrophys. J. 906, 73–100.
Hoang, T., Lazarian, A., 2016. A unified model of grain alignment: radiative alignment of interstellar grains with magnetic inclusions. Astrophys. J. 83, 159–179.
Hojou, K., Furuno, S., Kushita, K.N., et al., 1998. EELS analysis of SiC crystals under hyrogen and helium dual-ion beam irradtaion. Nucl. Intr. Meth. Phys. Res. B 141, 148–153.
Ishii, H.A., 2019. Comparison of GEMS in interplanetary dust particles and GEMS-like objects in a Stardust impact track in aerogel. Meteorit. Planet. Sci. 54, 202–219.
Ishii, H.A., Bradley, J.P., Dai, Z.R., et al., 2008. Comparison of comet 81P/Wild 2 with interplanetary dust from comets. Science 319, 447–450.
Ishii, H.A., Bradley, J.P., Bechtel, H.A., Brownlee, D.E., Bustillo, K.C., Ciston, J., Cuzzi, J. N., Floss, C., Joswiak, D.J., 2018. Multiple generations of grain aggregation in different environments preceded solar system body formation. Proc. Natl. Acad. Sci. 115, 6608–6613.
Jäger, C., Sabri, T., Wendler, E., Henning, Th., 2016. Ion-induced processing of cosmic silicates: a possible formation pathway to GEMS. Astrophys. J. 831, 66–74.
Jenkins, E.B., 2009. A unified representation of gas-phase element depletions in the interstellar medium. Astrophys. J. 700, 1299–1348.
Jones, A.P., 2016. Dust evolution, a global view: III. Core/mantle grains, organic nano-globules, comets and surface chemistry. Royal Soc. Open Sci. 3 (12), 160224.
Keller, L.P., Flynn, G.J., 2022. Evidence for a significant Kuiper belt dust contribution to the zodiacal cloud. Nature Astron 6, 731–735.
Keller, L.P., Messenger, S., 2011. On the origins of GEMS. Geochim. Cosmochim. Acta 75, 5336–5365.
Keller, L.P., Messenger, S., Bradley, J.P., 2000. Analysis of a deuterium-rich interplanetary dust particle (IDP) and implications for presolar material in IDPs. J. Geophys. Res. 165, 10397–10402.
Kimura, H., 2017. High radiation pressure on interstellar dust computed by light-scattering simulation on fluffy agglomerates of magnesium-silicate grains with metallic-iron inclusions. Astrophys. J. Lett. 839, L23–L27.
Koenderink, G.H., Brzesowsky, R.H., Balkenende, A.R., 2000. Effect of the initial stages of leaching on the surface of alkaline earth sodium silicate glasses. J. Non-Cryst. Solids 262, 80–98.
Krot, A.N., 2019. Refractory inclusions in carbonaceous chondrites: Records of early solar system processes. Meteorit. Planet. Sci. 54, 1647–1691.
Krot, A.N., Nagashima, K., Ciesla, F.J., Meyer, B.S., Hutcheon, I.D., Davis, A.M., Huss, G. R., Scott, E.R.D., 2010. Oxygen isotopic composition of the Sun and mean oxygen isotopic composition of the protoplanetary silicate dust: Evidence from refractory inclusions. Astrophys. J. 713, 1159–1166.
Leapman, R.D., Swyt, C.R., 1988. Separation of overlapping core edges in electron energy loss spectra by multiple-least-squares fitting. Ultramicroscopy 26, 393–403.
Leroux, H., Cuvillier, P., Zanda, B., Hewins, R.H., 2015. GEMS-like material in the matrix of the Paris meteorite and the early stages of alteration of CM chondrites. Geochim. Cosmochim. Acta 170, 247–265.
Love, S.G., Brownlee, D.E., 1991. Heating and thermal transformation of micrometeoroids entering Earth's atmosphere. Icarus 89, 26–43.
Love, S.G., Brownlee, D.E., 1996. Peak atmospheric entry heating temperatures of micrometeorites. Meteorit. Planet. Sci. 31, 394–402.
Lyons, J.R., Young, E.D., 2005. CO self-shielding as the origin of oxygen isotope anomalies in the early solar nebula. Nature 435, 317–320.
Martin, P.G., 1995. On the value of GEMS (glass with embedded metal and sulfides). Astrophys. J. 445, L63–L66.
Matsuno, J., Tsuchiyama, A., Mikaye, A., Nakamura-Messenger, K., Messenger, S., 2022. Three-dimensional observation of GEMS grains: their high-temperature condensation origin. Geochim. Cosmochim. Acta 320, 207–222.
Matsura, M., Dwek, E., Meixner, M., Otsuka, M., Babler, B., Barlow, M.J., Roman-Duval, J., Engelbracht, C., Sandstrom, K., Lakicevic, M., Van Loon, J. Th., Sonneborn, G., Clayton, G.C., Long, K.S., Lundqvist, P., Nozawa, T., Gordon, K. D., Hony, S., Panuzzo, P., Okumura, K., Misselt, K.A., Montiel, E., Sauvage, M., 2011. Herschel detects a massive dust reservoir in Supernova 1987A. Science 333, 1258–1261.
McKeegan, K.D., Kallio, A.P.A., Heber, V.S., Jarzebinski, G., Mao, P.H., Coath, C.D., Kunihiro, T., Wiens, R.C., Nordholt, J.E., Moses Jr., R.W., Reisenfeld, D.B., Jurewicz, A.J.G., Burnett, D.S., 2011. The oxygen isotopic composition of the Sun inferred from captured solar wind. Science 332, 1528–1532.
Messenger, S., 2000. Identification of molecular cloud material in interplanetary dust particles. Nature 204, 968–970.
Messenger, S., Keller, L.P., Stadermann, F.J., Walker, R.M., Zinner, E., 2003. Samples of stars beyond the solar system: Silicate grains in interplanetary dust. Science 300, 105–108.
Messenger, S., Nakamura-Messenger, K., Keller, L.P., Clemett, S.J., 2015. Pristine stratospheric collection of interplanetary dust on an oil-free polyurethane foam substrate. Meteorit. Planet. Sci. 50, 1468–1485.
Nakamura-Messenger, K., Clemett, S.J., Keller, L.P., Messenger, S., 2011. Experimental aqueous alteration of cometary dust. Meteorit. Planet. Sci. 46, 843–856.
Nittler, L.R., Stroud, R.M., Trigo-Rodríguez, J.M., de Gregorio, B.T.D., Alexander, C.M. O'D., Davidson, J., Moyano-Cambero, C.E., Tanbakouei, S., 2019. A cometary building block in a primitive asteroidal meteorite. Nature Astron. 3, 659–666.
Noguchi, T., Nakamura, T., Kimura, M., Zolensky, M.E., Tanaka, H., Hashimoto, T., Konno, M., Nakato, A., Ogami, T., Fujimura, A., Abe, M., Yada, T., Mukai, T., Ueno, M., Okada, T., Shirai, K., Ishibashi, Y., Okazaki, R., 2011. Incipient space weathering observed on the surface of Itokawa dust particles. Science 333, 1121–1125.
Noguchi, T., Yabuta, H., Itoh, S., Sakamoto, N., Mitsunari, T., Okubu, A., Okazaki, R., Nakamra, T., Tachibana, S., Terada, K., Ebihara, E., Imae, N., Kimura, M., Nagahara, H., 2017. Variation of mineralogy and organic material during the early stages of aqueous activity recorded in Antarctic micrometeorites. Geochim. Cosmochim. Acta 208, 119–1114.
Nguyen, A.N., Keller, L.P., Messenger, S., 2016. Mineralogy of presolar silicate and oxide grains of diverse stellar origins. Astrophys. J. 818, 51 (17 pp).
Ohtaki, K.K., Ishii, H.A., Bradley, J.P., Villalon, K.L., Davis, A.M., Stephan, T., 2021. Search for meteoritic GEMS I: Comparison of amorphous silicates in Paris and Acfer 094 chondrite matrices and in anhydrous chondritic interplanetary dust particles. Geochim. Cosmochim. Acta 310, 320–346.
Rietmeijer, F.J.M., 1987. Silicone oil: A persistent contaminant in chemical and spectral micro-analyses of interplanetary dust particles. Lunar Planet. Sci. 18, 836–837 (abstr.).
Rietmeijer, F.J.M., 2018. GEMS, hydrated chondritic IDPs, CI-matrix material: sources of water in 81P/comet Wild 2. Meteorit. Planet. Sci. 54, 259–266.
Rost, D., Stephan, T., Jessberger, E.K., 1999. Surface analysis of stratospheric dust particles. Meteorit. Planet. Sci. 34, 637–646.
Schramm, L.S., Brownlee, D.E., Wheelock, M.M., 1989. Major element composition of stratospheric micrometeorites. Meteoritics 24, 99–112.
Scott, J., Thomas, P.J., MacKenzie, M., McFadzean, S., Wilbrink, J., Craven, A.J., Nicholson, W.A.P., 2008. Near-simultaneous dual energy range EELS spectrum imaging. Ultramicroscopy 108, 1586–1594.
Shi, J., Wang, N., Gao, H., Baker, A.R., Yao, X., Zhand, D., 2019. Phosphorus solubility in aerosol particles related to particle sources and atmospheric acidification in Asian continental outflow. Atmos. Chem. Phys. 19, 847–860.
Stephan, T., 2001. TOF-SIMS in cosmochemistry. Planet. Space Sci. 49, 859–906.
Suttle, M.D., Genge, M.J., Foloc, L., Russell, S.S., 2017. The thermal decomposition of fine-grained micrometeorites, observations from mid-IR spectroscopy. Geochim. Cosmochim. Acta 206, 112–136.
Tencé, M., Pinna, H., Birou, T., Guiraud, L., Mayet, A., Pertel, C., Serin, V., Colliex, C., 2006. A new detector device designed for quantitative EELS spectroscopy. In: Ichinose, H., Sasaki, T. (Eds.), Proc. IMC 16, Sapporo, Japan, pp. 824–825.
Thomas, K.L., Blanford, G.E., Keller, L.P., Klock, W., McKay, D.S., 1993. Carbon abundance and silicate mineralogy of anhydrous interplanetary dust particles. Geochim. Cosmochim. Acta 57, 1551–1566.
Ueda, Y., Matsuda, K., Murakami, H., Matsushita, K., 2005. Study of the galactic interstellar medium from high-resolution X-ray spectroscopy: X-ray absorption fine structure and abundances of O, Mg, Si, S, and Fe. Astrophys. J. 620, 274–286.
van Boekel, R., Min, M., Leinert, Ch., et al., 2004. The building blocks of planets within the 'terrestrial' region of protoplanetary disks. Nature 432, 479–482.
van Boekel, R., Ratzka, T., Leinert, C., Henning, T., Min, M., Waters, R., 2005. The spatially resolved mineralogy of proto-planetary disks. In: Protostars and Planets V, p. #8448.
Vesavage, T., Thompson, A., Hausrath, E.M., Brantley, S.L., 2015. Basalt weathering in an Arctic Mars-analog site. Icarus 254, 219–232.
Villalon, K.L., Ohtaki, K.K., Bradley, J.P., Ishii, H.A., Davis, A.M., Stephan, T., 2021. Search for meteoritic GEMS II: Comparison of inclusions in amorphous silicates from the Paris chondrite and from anhydrous chondritic interplanetary dust particles. Geochim. Cosmochim. Acta 310, 346–362.
Voshchinnikov, N.V., Henning, T.h., 2010. From interstellar abundances to grain composition: the major dust constituents Mg, Si, and Fe. A & A 517, A45–A60.
Wiedenbeck, M.E., 2013. Elemental and isotopic composition measurements of galactic cosmic rays. AIP Conf. Proc. 1516, 150–155.
Yabuta, H., Noguchi, T., Itoh, S., Nakamura, T., Miyake, A., Tsujimoto, S., Ohashi, N., Sakimoto, N., Hashiguchi, M., Abe, K.I., Okubo, A., Kilcoyne, A.L.D., Tachibana, S., Ohazaki, R., Terada, K., Ebihara, M., Nagahara, H., 2017. Formation of an ultracarbonaceous Antarctic micrometeorite through minimal aqueous alteration in a small porous icy body. Geochim. Cosmochim. Acta 214, 172–190.
Ysard, N., Köhler, M., Jones, A., Dartois, E., Godard, M., Gavilan, L., 2016. Mantle formation, coagulation, and the origin of cloud/core shine II. Comparison with observations. Astron. Astrophys. 588, A44–A54.
Yurimoto, H., Kuramoto, K., 2004. Molecular cloud origin for the oxygen isotope heterogeneity in the solar system. Science 305, 1763–1766.
Zhukovska, S., Gail, H.-P., Trieloff, M., 2008. Evolution of interstellar dust and dust in the solar neighborhood. A & A 479, 453–480.
Zhukovska, S., Henning, T.h., Dobbs, C., 2018. Iron and silicate dust growth in the galactic interstellar medium: clues from element depletions. Astrophys J. 857, 94–106.